Atmos. Meas. Tech., 19, 7853–7884, 2026
https://doi.org/10.5194/amt-19-7853-2026
© Author(s) 2026. This work is distributed under
the Creative Commons Attribution 4.0 License.

Atmospheric Measurement Techniques
Open Access
EGU

# Aerodynamic evaluation of wind speed sensor placement on UAVs for meteorological applications

**Ashish Pastay**[1,2], **Shrivathsan Narayanan**[1,2], **and Bharath Govindarajan**[1,2]

[1]Department of Aerospace Engineering, Indian Institute of Technology Madras, Chennai, India
[2]Geophysical Flows Lab, Centre of Excellence, Chennai, India

**Correspondence:** Ashish Pastay (ashishpastay18@gmail.com)

Received: 19 February 2026 – Discussion started: 19 March 2026
Revised: 13 October 2026 – Accepted: 1 November 2026 – Published: 27 November 2026

**Abstract.** Vertical take-off and landing Unmanned Aerial Vehicles (VTOL-UAVs) can provide accurate, highly resolved, and repeatable atmospheric measurements, especially in scenarios where conventional measurement techniques are inadequate or impractical. Wind estimation using UAV-mounted sensors is significantly influenced and contaminated by rotor-induced flows, making its placement a critical design consideration for meteorological measurements. This work investigates candidate locations for wind speed sensor placement on various UAV systems by studying the rotor-induced flow field using a free-vortex wake model (FVM) across a single-rotor, quad-rotor, and hexa-rotor configurations under hover, axial descent, and forward descent flight conditions. This model is validated with an in-house experimental setup for velocity measurements. Care is taken to ensure these results are applicable across a wide range of practical UAV operating conditions through the dimensional disk loading (DL) parameter. The rotor-induced velocity fields are evaluated on multiple planes perpendicular to the rotor disk, and potential aerodynamic "quiet-zones" for sensor placement are identified based on a threshold of potential 1 % rotor-tip speed, with the sensor-accuracy boundary of $0.2\,\mathrm{m\,s^{-1}}$ additionally considered. Results reveal that the location and extent of the quiet-zones are strongly dependent on the flight condition. For single-rotor in hover, a well-defined potential aerodynamic quiet-zone exists above the rotor disk, while viable sensor placement locations are substantially reduced in axial descent. Forward descent introduces asymmetric wake skew, limiting quiet-zones to the upstream, at smaller axial distances. For multi-rotor configurations, the individual rotor hub locations and the system geometric centre lead to similar quiet-zone distances; therefore, the geometric centre is particularly suitable for sensor placement, considering structural and stability concerns. Overall, by analysing various rotor systems in different flight conditions, the present work provides practical guidance for the design of accurate UAV-based atmospheric measurement systems.

## 1 Introduction

Detection of wind is of paramount importance to our understanding of atmospheric dynamics, weather forecasting, climate monitoring, dispersion of contaminants and other allied phenomena, and applications. Meticulous observations of wind phenomena are particularly vital in inaccessible or data-scarce regions, where conventional observation methods fail to provide high accuracy wind data. Figure 1 shows a schematic of conventional wind sensing strategies and the typical altitudes where they are most effective. Traditionally used platforms such as weather balloons (Fujiwara et al., 2025) together with a radiosonde (Faber et al., 2023) are single-use and drift considerably with the wind, making it nearly impossible to obtain controlled and repeatable wind profile trajectories. Additionally, the wind velocity and direction estimated by these balloons may not be sensitive to high-frequency changes in the wind, because of the system's inertia and the consequent drifting of the balloon system. Aircraft-based observations (Gasch et al., 2023) are expensive and require significant infrastructure, making them less ideal for routine deployments in isolated or hazardous areas. Ground-based radar systems and profiling stations (Ritvanen et al., 2022) offer high-fidelity data but demand substantial

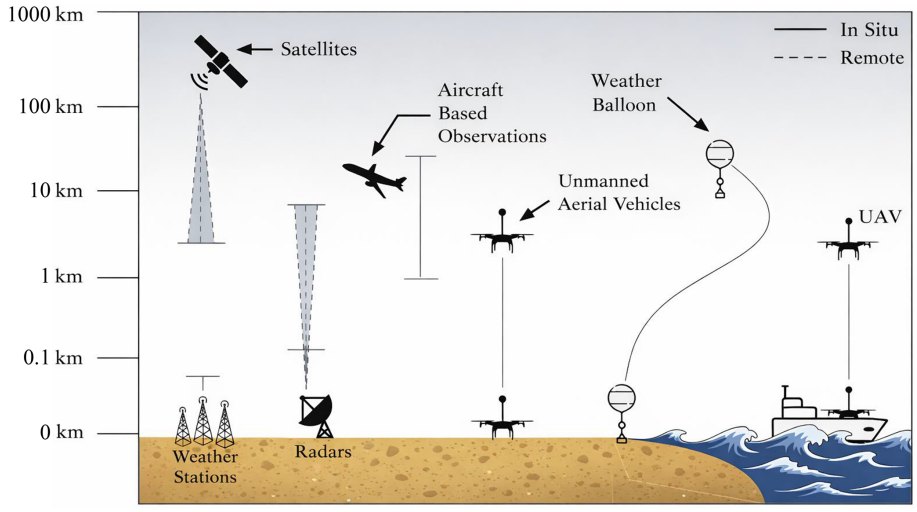


**Figure 1.** Conventional atmospheric sensing platforms and the potential role of UAVs.

investment; and these radar systems are also limited to land regions, rendering them ineffective over oceans or even remote mountainous terrains. Satellite-based wind sensing is effective over the upper regions of the atmosphere, but is sensitive to cloud cover (Stoffelen et al., 2005), which limits the spatial and temporal resolutions of the collected data. Furthermore, the data gathered depend on the trajectory of the satellite and the local atmospheric conditions.

In contrast, Unmanned Aerial Vehicles (UAVs, or drones) are a versatile and affordable option when used for in situ wind sensing. UAVs have been gaining attention in the meteorological and atmospheric measurement space, particularly for wind speed and direction measurements, wind profiling in the atmospheric boundary layer (ABL), and small-scale turbulence measurements (Hollenbeck et al., 2018; Thielicke et al., 2021; Jin et al., 2024; Ghirardelli et al., 2025). Because of their lower cost compared to other strategies and relatively smaller size, they can be deployed repeatedly and selectively to measure the desired wind profiles. They can accommodate mission-specific requirements, can be programmed to follow controlled trajectories, and can carry out high-resolution wind profiling at user-specified altitudes. These merits of UAVs can complement conventional atmospheric sensing platforms, wherever the latter is not effective or unable to obtain valid measurements. Of the many atmospheric science questions that remain unanswered, understanding of the various phenomena prevalent in the ABL, i.e., within 5 km above mean sea level (Witte et al., 2017), still remains one of the most important frontiers in the domain of meteorological studies; and the ability of UAVs to obtain atmospheric data within the ABL presents them as a potential candidate to bridge current observational gaps and improve data coverage in remote environments.

A key question that arises in using UAVs to carry out measurements of wind velocity and direction is the placement of a wind speed sensor, particularly in configurations that feature rotors/propellers. It is known that these rotary wing systems entrain the flow around them and there is a velocity field that develops in the vicinity of the rotor (Leishman, 2006a). The nature of these flow fields, i.e., the magnitude of velocity and its "hotspots" relative to the rotor/propeller, is dependent on the size of the rotors, the thrust they generate, and the flight condition. On one hand, if the wind speed sensor is placed significantly close to the rotors, it is affected by the complicated aerodynamic environment surrounding the system, particularly the flow that is entrained through the rotor disk which would corrupt the wind signals. However, if the sensor is placed considerably far away from the rotors, it is no longer affected by the flow around the rotor; but the inertia of the system shifts towards the sensor, leading to poor vehicle stability and handling concerns during flight. Such issues only amplify and create additional challenges in unsteady or gusty conditions. Therefore, perhaps there exists an optimal location of the wind-sensor placement that allows for accurate measurement of the wind while maintaining sufficient control authority of the UAV. The present work focuses on the aerodynamics of this problem, while recognising that a detailed account of the relevant control aspects is necessary but out of scope of the current investigation.

Figure 2 shows the various types of UAV-mountable wind speed sensors based on different measurement principles. The pitot-static tube (Fig. 2a) is used to measure airspeed from the pressure difference between its stagnation and static ports; pitot-tubes can be used to approximate the wind vector if combined with the ground speed obtained from GPS systems (Cho et al., 2011). The mechanical cup anemometer (Fig. 2b) is a wind speed measurement system based on the rotational speed of a set of hemispherical cups that rotate at a rate proportional to the wind velocity. The cup anemometer is typically calibrated by magnetic or optical encoders



(a) (b) (c) (d)

**Figure 2.** Representative UAV-mountable wind sensors based on different measurement principles: **(a)** pitot–static tube (NW Blue, 2026), **(b)** mechanical cup anemometer (PCE Instruments, 2026), **(c)** thermal (hot-film) anemometer (Modern Device, 2026), and **(d)** 3D ultrasonic anemometer (LI-COR Environmental, 2026). Product images are sourced from the respective manufacturers.

(Pindado et al., 2014). The thermal (hot-film) anemometer (Fig. 2c) determines the flow velocity from the cooling rate of a heated filament exposed to the flow. The voltage supplied to the filament is adjusted to maintain a steady temperature, and the flow velocity is calculated using a calibration procedure; the hot-film anemometer is highly effective when measuring the wind velocity in turbulent flow, but the sensor does not inherently indicate the flow direction (Inoue and Sato, 2022; Simon et al., 2022). The 3D ultrasonic anemometer (Fig. 2d) measures wind velocity magnitude and direction by determining the transit-time differences of ultrasonic pulses between transducers. All components of velocity can be directly estimated with high temporal resolution and minimal flow disturbance, making it very suitable for accurate wind measurements on UAV platforms (Hollenbeck et al., 2018; Thielicke et al., 2021; Basawanal et al., 2025).

Recent investigations have been conducted into the placement of atmospheric sensors for UAV-based measurements that examine the influence of propeller-induced flow; however, the general body of literature remains limited. Wilson et al. (2022) combined laboratory Particle Image Velocimetry (PIV) measurements with field experiments on a quadcopter platform to characterise rotor-induced velocities above the UAV. It was shown that placing sensors approximately 5.3 rotor diameters above the rotor plane yields wind speed measurements that closely match mast-mounted references, with differences within 5.5 % and preserved spectral characteristics. Ghirardelli et al. (2023) quantified propeller-induced flow effects on UAV-mounted wind sensors using normalised wind speed deviation metrics in a Computational Fluid Dynamics (CFD) study of a coaxial multi-copter. For the specific platform utilised in the study, regions of minimal flow disturbance were identified upstream and below the rotor plane, corresponding to horizontal and vertical offsets of approximately 0.46–1.66 and 0.01–0.70 rotor diameters, respectively. Thielicke et al. (2021) developed a custom rotary-wing UAV equipped with a full-scale ultrasonic anemometer and validated its performance through calibration wind-tunnel experiments, large-scale wind-tunnel tests with operating rotors, and field comparisons against bistatic Doppler LiDAR. Wind velocity was reconstructed as the total wind vector using data fusion of measured relative velocity and UAV kinematics. The propeller-induced effects were explicitly isolated and corrected for the UAV platform considered in the study, and a negligible influence on horizontal velocity was observed when the sensor was mounted approximately 2.5 rotor diameters above the rotor plane. However, the study does not provide a generalised or scalable framework for predicting propeller-induced effects or optimising sensor placement across different multi-rotor geometries and operating conditions. In another study, Jin et al. (2024) employed Reynolds-averaged CFD validated using tri-beam Doppler LiDAR measurements to quantify propeller-induced effects through normalised deviations of horizontal wind speed relative to freestream velocity. Their analysis showed that the regions of minimum flow distortion are located upstream of the UAV and below the rotor plane. Under a stringent disturbance criterion of 1 % of velocity, the vertical wind component remained affected even at an upstream separation distance of approximately 5 m (about 7 rotor diameters), corresponding to a boom length that is impractical for a multicopter with a rotor diameter of 0.71 m and an overall span of 1.88 m. When a less restrictive threshold of 5 % velocity deviation was adopted, the required upstream separation reduced to approximately 2 m at ambient wind speeds exceeding 4 m s$^{-1}$. More recently, Ghirardelli et al. (2025) presented the SAMURAI-S system, in which a research-grade ultrasonic anemometer is suspended as a sling load of approximately 18 m ($\sim$ 26 rotor diameters) below a multi-rotor UAV to completely eliminate propeller-induced effects. While this configuration enables accurate measurements of total wind and turbulence, the sensor was intentionally positioned far from the UAV frame and therefore does not inform practical near-body sensor placement strategies for compact multi-rotor platforms.

Collectively, these studies demonstrate the importance of understanding rotor wake characteristics for appropriate sensor placement; however, the reliance on expensive computational and/or experimental infrastructure limits their applicability to multi-rotor configurations and large parametric studies. Furthermore, although commercial UAV-based atmospheric measurement platforms are available (Menapia Ltd.,

2026; Meteomatics, 2026), detailed and publicly available information regarding their wind sensor placement strategies remains scarce, underscoring the need for systematic and cost-effective investigation.

In summary, it is crucial to understand the aerodynamic disturbances generated by UAV rotors in their vicinity to fully exploit the potential of UAV-mounted wind speed sensors for meteorological applications. Identifying potential aerodynamic "low-disturbance zones" or "quiet-zones" around a UAV is of fundamental importance for sensor placement and accurate wind measurement. The dearth of publicly available information on state-of-the-art UAV wind measurement systems underscores the need for systematic studies to identify aerodynamically effective sensor placement strategies that minimise the influence of rotor-induced flow. Although CFD studies in the literature have provided some insight, as a tool, CFD is computationally expensive to sweep through a wide variety of UAV configurations and operating conditions.

The focus of the present study is to use an alternate relatively parsimonious model (based on vortex methods), which presents the possibility of performing analyses on a vast array of scenarios. Specifically, an in-house free-vortex wake model (FVM) is used to analyse the wake behaviour of UAV-scale rotor systems under different flight and thrust conditions to identify candidate zones for wind sensor placement. The study is performed on an isolated rotor, a quad-rotor, and a hexa-rotor configuration of a UAV-scale propeller. To validate the wind speed measurements, a supporting experimental setup is also utilised. The setup employs an ultrasonic anemometer (TriSonica Mini wind and weather sensor, shown in Fig. 2d) for wind velocity measurements, chosen for its reliable low-speed response, high temporal resolution, and direct three-component velocity measurement with minimal flow distortion. All results designated as "sensor boundary" throughout this work are calculated based on the specifications of the TriSonica Mini wind and weather sensor. Corresponding modifications can be incorporated into any UAV-based meteorological platform, depending on the wind speed measurement sensor utilised.

## 2 Methodology

### 2.1 Free-vortex wake model (FVM)

FVMs are a class of mid-fidelity numerical tools specifically tailored to simulating vortex-dominated flows and capture key rotorcraft flow field features. They lie between the traditional low-fidelity dynamic inflow models (Lee et al., 2022) and more expensive high-fidelity CFD approaches (Datta et al., 2007) to analyse the aerodynamics of rotor systems. FVMs offer a trade-off between solution accuracy and computational efficiency (Zanotti et al., 2021), making them suitable for analysing complex multi-rotor configurations, involving large parameter sweeps. Several flow field intricacies such as blade-vortex interactions are efficiently captured by FVMs (Romani and Casalino, 2019), adding to their credibility in solving unsteady rotorcraft aerodynamic problems. Furthermore, low-fidelity inflow models are not suitable for descent flight conditions (as they cannot capture the complex rotor wake interactions), which are also of considerable interest in this study. The model developed by the authors for an earlier work (Narayanan and Govindarajan, 2024) has been utilised for the present study, and a few key parameters of the developed model are detailed below.

#### 2.1.1 Governing equations

The governing equation for the FVM model is the velocity-vorticity form of the Navier-Stokes equation, which is solved under the assumption of potential flow (Bhagwat and Leishman, 2000; Leishman et al., 2002). The convection of free vortices is described by

$$\frac{\mathrm{d}\boldsymbol{r}}{\mathrm{d}t} = \boldsymbol{V}(\boldsymbol{r}) \tag{1}$$

where $\boldsymbol{r}$ denotes the position vector of a point in the rotor wake, and $\boldsymbol{V}(\boldsymbol{r})$ represents the local fluid velocity at that point (Bhagwat and Leishman, 2000). Expressing the system in terms of the azimuthal position of the blade ($\psi$), the wake age ($\zeta$) and the angular velocity of the rotor ($\Omega$), the governing equation is reformulated as

$$\frac{\partial \boldsymbol{r}}{\partial \psi} + \frac{\partial \boldsymbol{r}}{\partial \zeta} = \frac{\boldsymbol{V}(\boldsymbol{r})}{\Omega} \tag{2}$$

Equation (2) is numerically solved using a second-order predictor-corrector (PC2B) method (Bhagwat and Leishman, 2000). Figure 3a presents a schematic representation of the FVM formulation adopted in this study. Each rotor blade is discretised into 40 span-wise blade elements, and the unsteady aerodynamic loads on each element are computed using Blade Element Theory (BET), and a solution to the Duhamel integral (Leishman, 2006b), resulting in time-varying lift and drag coefficients $C_{\mathrm{l}}(t)$ and $C_{\mathrm{d}}(t)$. For all studies, a time-step equivalent to a 10° sweep of the blade is chosen, and at each time step, changes in bound circulation are shed into the wake as free-vortex filaments (Leishman et al., 2002). For numerical efficiency, the continuously curved wake is approximated using straight-line vortex segments generated over a 30° azimuthal interval (Bhagwat and Leishman, 2001). The wake is represented using Lagrangian markers, which denote the discrete spatial locations of the endpoints of the vortex filament and are convected in the Lagrangian framework under the local velocity field (Bhagwat and Leishman, 2000; Ananthan and Leishman, 2004). The typical wake structure beneath the rotor/propeller is helical in nature as seen in Fig. 3b (Bauknecht et al., 2014) (adapted with permission), and consequently, in this study, six turns are retained.

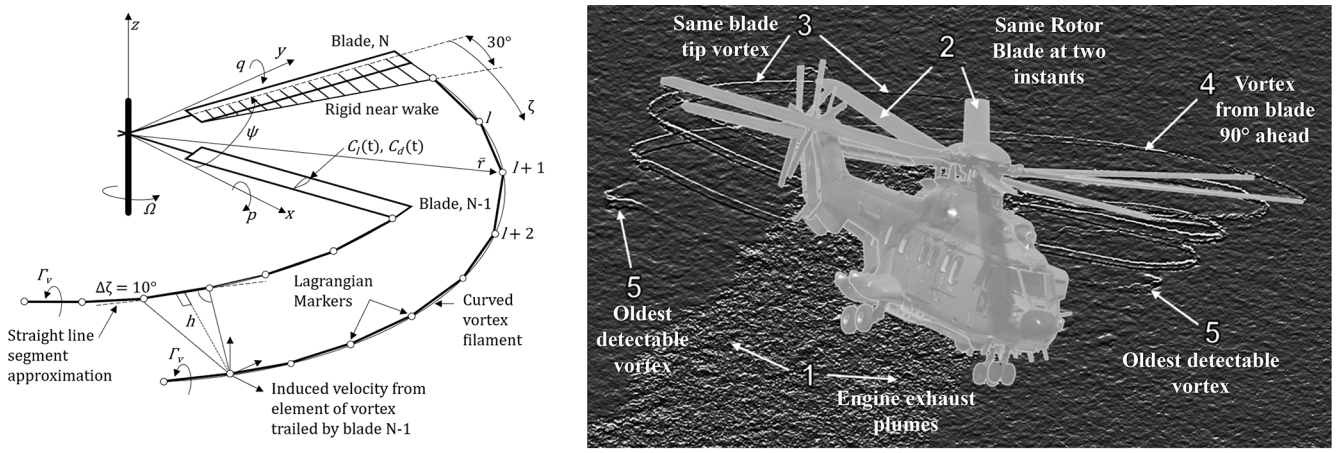


(a) (b)

**Figure 3.** Representative rotor wake structures in a typical rotorcraft aerodynamic environment: **(a)** rotor blade discretisation and near-wake structure used in the FVM model; **(b)** helical blade-tip vortex wake structure of a Cougar helicopter visualised using the background-oriented Schlieren (BOS) technique (adapted from Bauknecht et al., 2014 with permission).

### 2.1.2 Induced velocity calculations

Within the FVM formulation, the induced velocity at any point in space, at a given time step, is obtained by a vectorial summation of the contributions of all vortex filaments trailed into the rotor wake. This induced velocity $\boldsymbol{v}_i$ due to the vortex filament at a control point $\boldsymbol{r}$ is given according to the Biot–Savart law (Fig. 4a) as

$$\boldsymbol{v}_i(\boldsymbol{r}) = \frac{\Gamma}{4\pi} \int_{\text{filament}} \frac{\mathrm{d}\boldsymbol{l} \times (\boldsymbol{r} - \boldsymbol{r}')}{|\boldsymbol{r} - \boldsymbol{r}'|^3} \tag{3}$$

where $\Gamma$ denotes the strength of the vortex, $\mathrm{d}\boldsymbol{l}$ is the elemental vortex segment, and $\boldsymbol{r}'$ represents the source point on the vortex filament. In the present formulation, the rotor wake vortices are discretised into finite straight-line segments, and the induced velocity is computed by accumulating the contributions of all such segments, at any given time step. This induced velocity calculation is used to identify the potential aerodynamic quiet-zone for wind sensor placement. A representative schematic of the rotor wake, a target plane, and the calculation of the induced velocity is shown in Fig. 4b.

## 2.2 Experimental Setup

An in-house experimental setup, as shown in Fig. 5, is utilised to validate the velocity predictions from the FVM model. The setup houses a single-rotor commercial APC $12 \times 6$E UAV-scale propeller (APC Propellers, 2026) with a diameter of 0.3048 m (12 in.), mounted horizontally (parallel to the ground) on a rotor test rig. The rotor is driven by a T-Motor AT2317 KV880 Long Shaft Brushless DC (BLDC) motor (T-Motor, 2026), powered by an 8000 mA h battery with an output of 11.1 V. Experiments were conducted in a laboratory measuring $10\,\mathrm{m} \times 5\,\mathrm{m} \times 3\,\mathrm{m}$, on a test rig whose cast iron base measures $1.2\,\mathrm{m} \times 1.0\,\mathrm{m}$. The motor-propeller assembly is mounted on this test rig base at a height of $\approx 1\,\mathrm{m}$ from the ground. The support structure is an open cubical frame constructed using $0.04\,\mathrm{m} \times 0.04\,\mathrm{m}$ aluminium extrusion profiles. Rotor-induced velocity is measured using the TriSonica Mini weather sensor mounted on a movable aluminium extrusion profile of identical cross-section. Particular care is taken to ensure that no external intrusions block the measurement domain.

The TriSonica Mini wind and weather sensor (referred to as the "sensor") is positioned along the rotor axis to measure the rotor-induced velocity at various upstream and downstream locations. The sensor is capable of recording flow speeds in the range of 0–50 m s$^{-1}$ with an accuracy of ±2 %–4 % and a resolution of 0.01 m s$^{-1}$. In this work, the maximum possible data acquisition rate of the sensor, 40 Hz, is utilised. In addition to the velocity magnitude, the sensor reports the wind velocity through three orthogonal components $(u, v, w)$, as illustrated in Fig. 5, resolved to 1°. The components $u$ and $v$ cover 0–359° with an angular accuracy of ±1°, while the component $w$ measures deviations up to ±15° from the horizontal, with an accuracy of 0.2 m s$^{-1}$. The sensor is oriented such that its North direction faces the propeller. Accordingly, the positive $u$-component corresponds to flow from the North direction, i.e., from the propeller towards the sensor, while the positive $v$-component corresponds to flow from the East direction. The positive $w$-component represents vertically upward flow. Although all three components are recorded by the sensor, only the $u$ and $v$ components are utilised in the present analysis. The $w$-component is excluded because its measurement range is limited and its accuracy is affected by blockage effects associated with the sensor. Before each test, the sensor was calibrated under quiescent ambient conditions to ensure reliable measurements.

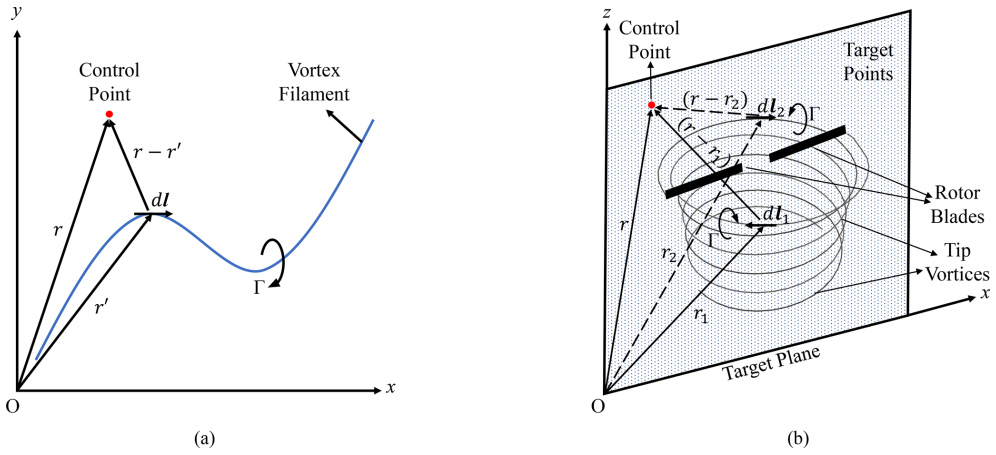


**Figure 4.** Induced velocity computation using the Biot–Savart law: **(a)** induced velocity evaluation at a control point due to a vortex filament; **(b)** induced velocity calculations on a representative target plane using discretised vortex segments.

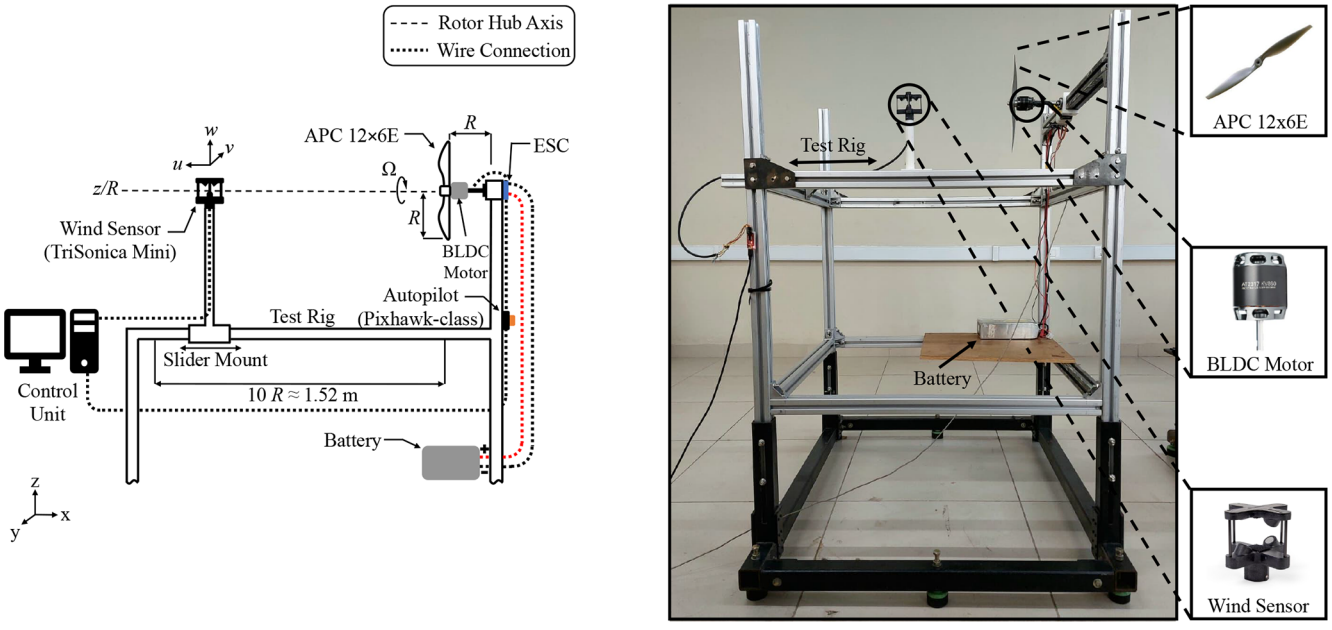


**Figure 5.** Schematic representation and actual image of the experimental setup and instrumentation used in the present study.

## 3 Results and Discussions

This section presents the results of the present study in the following order

1. Cross-validation of the rotor-induced velocity between the in-house developed FVM solver and the experimental facility.
2. Numerical studies of the flow field of the rotor in single, quad and hexa-rotor configurations of APC 12 × 6E (APC propeller) to identify the optimal location for the placement of the wind speed sensor.

Prior to analysing these results, it is critical to recognise that rotors and their operating conditions on UAVs span a wide range. Consequently, there is a need for an effective parameter that can systematically describe UAVs spanning different weight and size classes. One such parameter from the field of rotorcraft is disk loading (DL), which is defined as the ratio of the total thrust ($T$) generated by a rotor to the total area ($A$) of the rotor disk.

$$\mathrm{DL} = \frac{T}{A} \tag{4}$$

where $A = \pi R^2$ and $R$ is the radius of the rotor. Disk loading is an appropriate physically meaningful and practically grounded parameter that enables generalisation of the oper-

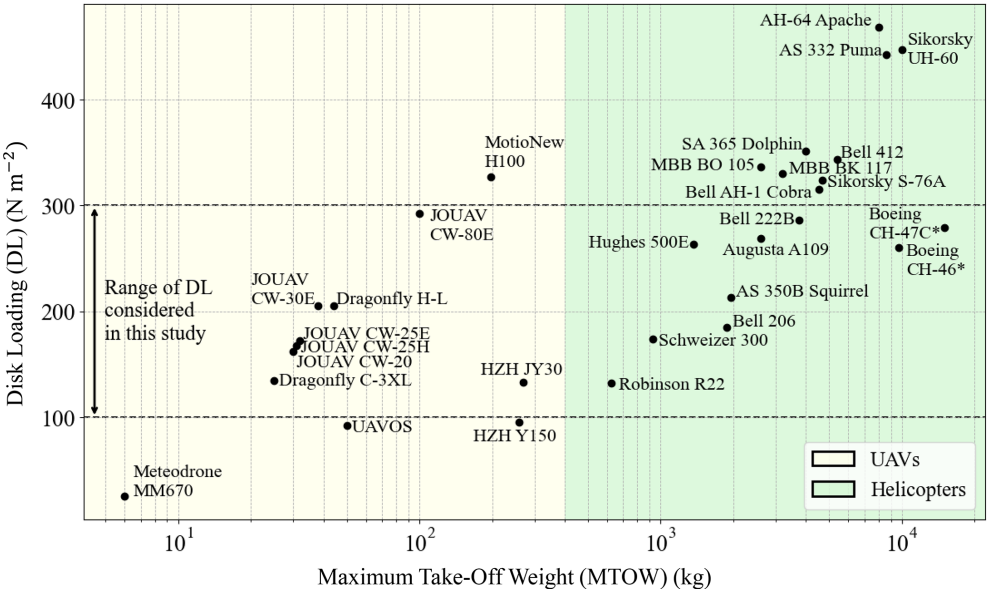


**Figure 6.** Disk Loading (DL) (N m$^{-2}$) vs. Maximum Take-Off Weight (MTOW) (kg) for a range of UAVs (yellow) and helicopters (green). The typical DL range of 100–300 N m$^{-2}$ for UAVs motivates its use in our study; the corresponding rotorcraft data sources are provided in Appendix A.

ating thrust condition of rotor systems across scales – from electrically driven small-scale UAV rotors to large-scale helicopter systems, as shown in Fig. 6. However, it is a dimensional parameter (with units of force per length$^2$), in contrast to the typically utilised non-dimensional parameters for cross-scale generalisation in aerodynamics. Appendix B evaluates the suitability of DL for comparing rotors of different scales by examining how changes in rotor solidity, blade number, and tip Mach number affect the predicted induced velocity profiles. To ensure relevance and applicability of the present study to real-world systems, the distribution of disk loading was examined across a variety of commercially available UAVs and helicopter platforms. Two categories are introduced based on the Maximum Take-Off Weight (MTOW) of the rotorcraft: 1. UAVs (yellow shaded region) – These include electrically driven small-to medium-scale vehicles with MTOW typically below 100 kg, and 2. Full-scale helicopters (green shaded region) – these encompass conventional combustion engine-driven vehicles with MTOWs often in excess of 1000 kg.

It is evident from Fig. 6 that most commercially available UAVs, irrespective of the vehicle's specific configuration, operate within a DL range of $\approx$ 100–300 N m$^{-2}$ – primarily due to design constraints related to electric propulsion, battery limits, and aerodynamic efficiency. Such a trend is also visible in the helicopter regime. Consequently, for the present study, a DL range of 100–300 N m$^{-2}$ was considered as it captures realistic operating conditions for a wide class of UAVs.

**Propeller Geometry**

The APC 12 $\times$ 6E UAV-scale propeller was utilised in this study for validation and sensor placement studies. The spanwise twist and chord distributions of the APC propeller are presented in Fig. 7, and other geometry and flow parameters for the various rotor configurations considered in the study are detailed in Table 1. These values are obtained from the now publicly available specification sheets provided by the manufacturer APC Propellers (2026). Sectional aerodynamic computations are carried out by approximating the blade sections as a modified National Advisory Committee for Aeronautics (NACA) 0012 airfoil with a 2° zero-lift angle of attack (see Appendix C2).

## 3.1 Validation

### 3.1.1 Single-rotor validation

The developed FVM model has been validated in the previous work by the authors Narayanan and Govindarajan (2024) for the steady-state thrust characteristics of the full-scale Harrington single and coaxial-rotors (see Appendix C1), performance characteristics of the UAV-scale APC 12 $\times$ 6E single-rotor (see Appendix C2), and the unsteady thrust response to pitch-rate changes of the full-scale Carpenter–Fridovich single-rotor (see Appendix C3). The FVM investigations of the APC single-rotor thrust and power characteristics (see Appendix C – Fig. C1b) and Fig. C1c demonstrated good agreement with the corresponding manufacturer data for the propeller.

**Table 1.** Geometry and flow details of the APC single, quad, and hexa-rotor configurations.

| Parameters | Single-rotor | Quad-rotor | Hexa-rotor |
|---|---|---|---|
| Blade Radius, $R$ (m) | 0.1524 | 0.1524 | 0.1524 |
| Root cutout, $r_0$ (% $R$) | 18.33 | 18.33 | 18.33 |
| Chord, $c(r)$ (m), and Twist, $\theta_{tw}(r)$ (°) | See Fig. 7 | See Fig. 7 | See Fig. 7 |
| Collective Pitch, $\theta_0$ (°) | 5.6168 | 5.6168 | 5.6168 |
| Number of blades, $N_b$ per rotor | 2 | 2 | 2 |
| Number of rotors, $N_r$ | 1 | 4 | 6 |
| Inter-rotor disk spacing, (% $R$) | ... | 10 | 10 |
| Angular Velocity, $\Omega$ (rad s$^{-1}$) | 516–900 | 516–900 | 516–900 |
| Tip Mach Number, $M_{tip}$ | 0.231–0.403 | 0.231–0.403 | 0.231–0.403 |

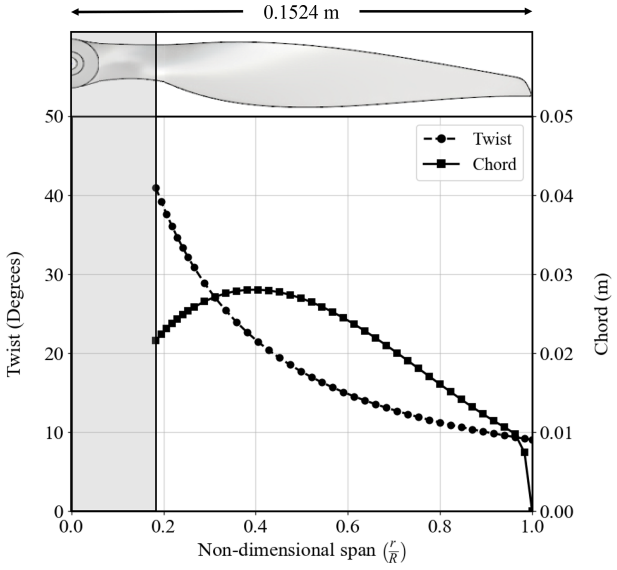


**Figure 7.** Span-wise twist and chord distributions of the APC propeller.

To further strengthen the credibility of the developed FVM model beyond force predictions, the rotor wake-induced velocity obtained from FVM was compared against the in-house experimental results obtained using the TriSonica Mini wind sensor. For both the numerical and experimental analyses, the APC 12 × 6E single-rotor was operated in hover, at a representative DL of 100 N m$^{-2}$. Accordingly, the rotor was simulated at an angular speed of 4695 RPM (491.66 rad s$^{-1}$) for the FVM simulations obtained from the performance characteristics validation – Appendix C, Fig. C1b, while a ±50 RPM (±5.23 rad s$^{-1}$) tolerance was accepted for the experiments. Two distinct cases are presented: axial variation of the induced velocity along the hub of the single-rotor; a two-dimensional spatial validation of the induced velocity across the span of the propeller at various axial streamwise locations, to validate the FVM model for predicting quiet-zones. The measurement domain for the spatial validation were defined in the $x$–$z$ plane over the same $x/R$ and $z/R$ ranges for both the experiments and FVM (here, $x$ is the span-wise coordinate axis, while $z$ is the axis of rotation of the propeller).

As shown in Fig. 8, the experimental measurements (Fig. 8a) were obtained at 105 discrete locations distributed uniformly across the domain using the TriSonica Mini sensor, with a positioning accuracy of $\approx \pm 0.005$ m, while the FVM calculations (Fig. 8b) were performed on a 100 × 100 equispaced Cartesian grid, resulting in 10 000 target locations. Furthermore, a sensitivity analysis was also performed for the various FVM parameters considered in the simulations to establish the convergence in induced velocity predictions. Detailed explanation of this study is given in Appendix D, with the baseline parameters highlighted in Table D1 held constant throughout all numerical simulations. Experimentally, at each measurement location, three independent trials of 30 s duration were conducted, with 10 s of the ambient flow condition recorded prior to the rotor-induced velocity measurements. From each 30 s measurement, 15 s of the induced velocity data were retained for analysis, after ensuring the transients had settled to achieve the desired operating condition. The corresponding mean ambient velocity was subtracted from the measured velocity at each location to account for background laboratory flow. The ambient-corrected measurements were then evaluated both on a trial-wise basis and collectively to obtain the ensemble mean and associated standard deviation.

Figure 9 presents the experimental validation of the induced velocity distribution predicted by the FVM model for the APC 12 × 6E single-rotor operating in hover at DL = 100 N m$^{-2}$. The axial variation of the induced velocity along the rotor hub is shown in Fig. 9a. The two-dimensional spatial distribution of the induced velocity is presented in Fig. 9b, specifically highlighting the various potential aerodynamic quiet-zone boundaries. In both cases, the induced velocity is evaluated as the magnitude of the time-averaged velocity components, $V_{ind} = |\langle V_{ind} \rangle|$; this metric ($V_{ind}$) is utilised consistently throughout this work for all induced velocity computations. The velocity statistics reveal that for both the experimental and numerical results, fluctuations in the induced velocities are small, the extrema are bounded

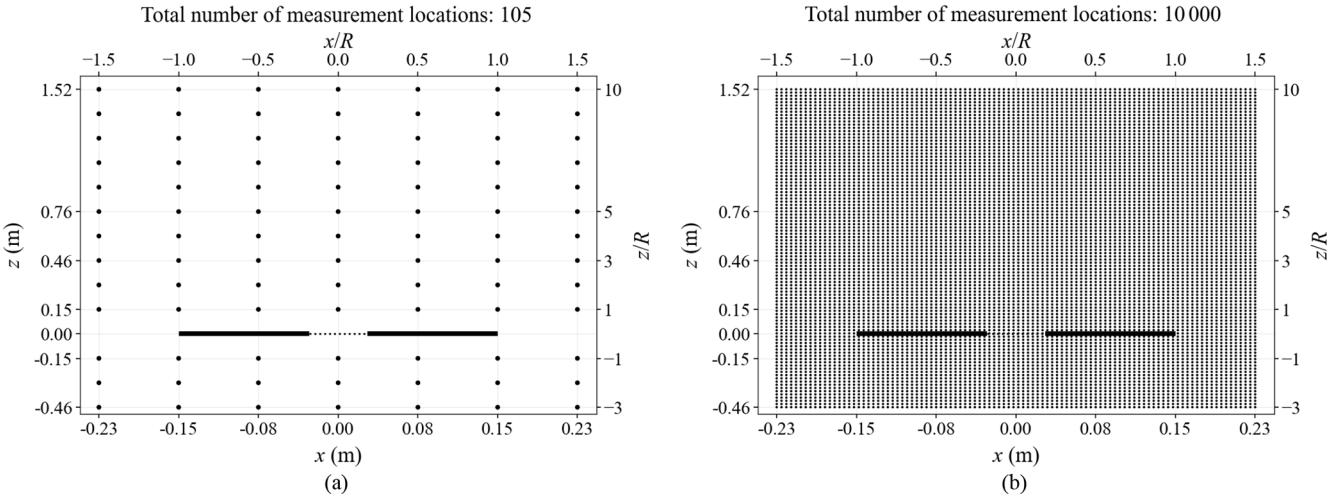


**Figure 8.** Measurement locations for the validation of the spatial distribution of the induced velocity on the APC single-rotor: **(a)** 105 discrete locations used for the experimental measurements and **(b)** 10 000 locations generated using a $100 \times 100$ equispaced grid for the FVM calculations over the same $x/R$ and $z/R$ ranges.

within a narrow distribution, indicating that the large amplitude fluctuations are not cancelled out. Therefore, the mean and standard deviation of the velocity serve as the necessary and perhaps sufficient quantities to characterise the induced velocity field for this study.

Figure 9a shows the variation of the tip speed normalised rotor-induced velocity ($V_{\text{ind}}/V_{\text{tip}}$) with the non-dimensional axial position $z/R$. Here, positive $z/R$ denotes locations above the rotor disk plane and negative values denote locations below it. The experimental results comprise three independent trials, represented by grey markers, with the corresponding $1\sigma$ variation. The ensemble mean obtained with data over all three trials (indicated by black markers) is also presented with the associated $1\sigma$ variation, and is utilised for the subsequent spatial validation of the induced velocity. The solid black curve represents the FVM predictions, with the corresponding $1\sigma$ standard-deviation band shaded in grey. The three experimental trials exhibit good repeatability, particularly above the rotor disk, providing confidence that the measured axial profile is not strongly affected by trial-to-trial variability or large statistical fluctuations. Furthermore, the FVM predictions show good agreement with the experimental measurements above the rotor disk, which is the region of primary interest for sensor placement. The agreement becomes less pronounced below the rotor plane, where the experimental measurements are associated with a highly turbulent rotor wake (characterised by viscous effects, vortex merging, or vortex breakdown), which the potential-flow based FVM formulation does not explicitly model. This discrepancy in the prediction of the wake-induced velocity, while significant for characterising the properties of the rotor wake, does not influence the prediction of the time-averaged induced velocity above the rotor disk, rendering the FVM model capable of identifying candidate sensor placement locations.

The two-dimensional spatial distribution of the rotor-induced velocity was compared between the experimental results and the FVM predictions to test the ability of the FVM model in identifying potential aerodynamic quiet-zones. The ensemble mean of the ambient-corrected experimental data over the three trials was computed at each measurement location, while the time-averaged induced velocity from the FVM model was directly utilised. Figure 9b depicts the spatial induced velocity distribution with a $0.01V_{\text{tip}}$ threshold and a $0.2\,\text{m}\,\text{s}^{-1}$ TriSonica Mini sensor-accuracy boundary applied to both the experimental and FVM velocity fields. Experimental measurements are not available within $(-R, R)$ due to mechanical constraints that prevent placing the sensor close to the propeller; the missing values in this region are therefore obtained through linear interpolation of the velocity data between the measured locations. In general, the discrete dataset in both experiments are the FVM data are linearly interpolated to obtain the smooth contour maps presented throughout this study. It is also important to note that the experimental data are subject to the sensor uncertainty of approximately $\pm 0.2\,\text{m}\,\text{s}^{-1}$. Along with these considerations, both the experimental and FVM results demonstrate close agreement in the predicted extent of the potential aerodynamic quiet-zone above the APC single-rotor. In particular, both the experimental and FVM predictions place the $0.01V_{\text{tip}}$ boundary at approximately $z/R = 1.8$ along the rotor axis, while the $0.2\,\text{m}\,\text{s}^{-1}$ sensor boundary also shows reasonable agreement.

It is pertinent to note that the maximum sampling frequency of the TriSonica Mini sensor is 40 Hz, (yielding a Nyquist limit of 20 Hz). The blade-passage frequencies for the rotor operating conditions considered in the present vali-

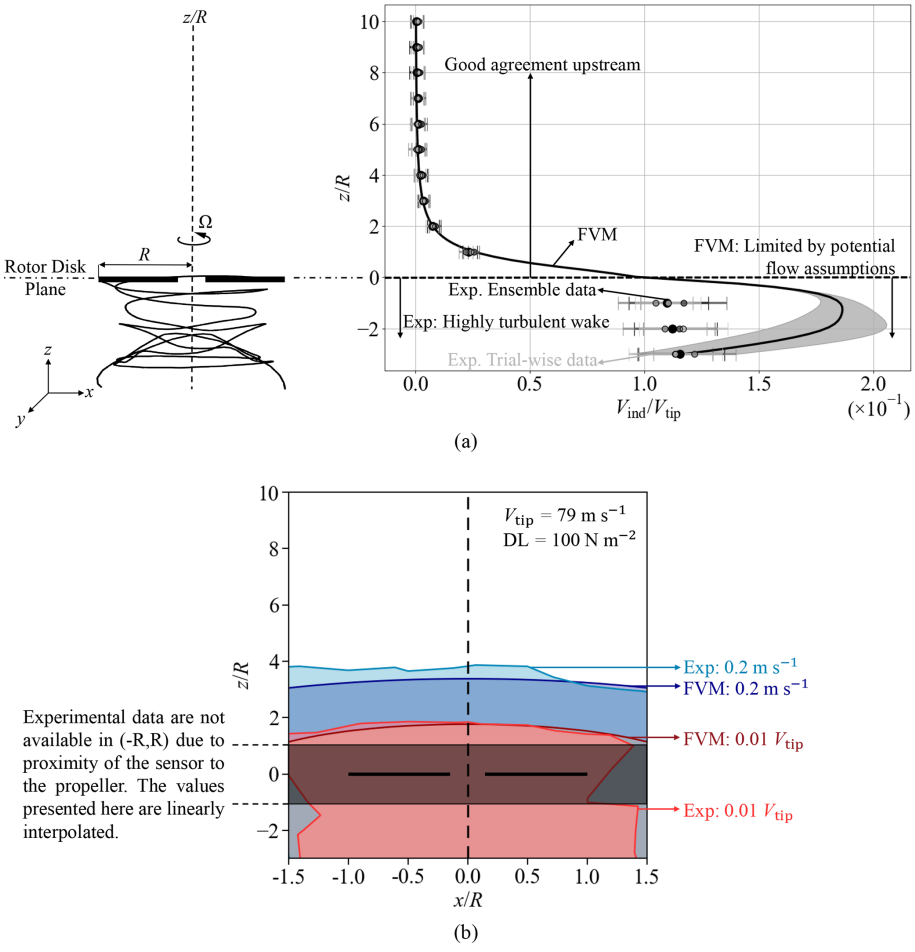


**Figure 9.** Validation for the APC single-rotor in hover at DL = 100 N m$^{-2}$: **(a)** axial induced velocity profile along the rotor hub obtained from experiments and the FVM model showing trial-wise and ensemble results. Shown on the left is the time-averaged wake representation of the rotor system from the FVM model; **(b)** comparison of $0.01\,V_{tip}$ threshold and 0.2 m s$^{-1}$ sensor-accuracy boundary for the identification of potential aerodynamic quiet-zones obtained from two-dimensional spatial measurements from experiments and FVM.

dation are ≈ 150–250 Hz – substantially higher than the sensor sampling frequency. Therefore, the blade-passage harmonics and higher "rev$^{-1}$" components cannot be resolved by the experimental setup and may be aliased into the lower-frequency spectrum. However, the focus of the present validation lies strictly on evaluating the time-averaged rotor-induced velocity rather than the resolved unsteady rotor harmonics. The high-frequency fluctuations predicted by the numerical model are also predominantly localised within the rotor wake, whereas the upstream region relevant to candidate sensor placement exhibits comparatively stable velocity magnitudes. Thus, the unresolved high-frequency content is expected to have a negligible influence on the time-averaged induced velocity used to identify the potential aerodynamic quiet-zones.

Overall, the axial and spatial comparisons establish considerable agreement between the FVM predictions and the experimental measurements for the single-rotor hover case. Over the range $z/R \in (1, 10)$, the mean absolute difference between the FVM and ensemble experimental values of $V_{ind}/V_{tip}$ is approximately 0.001 % of the rotor-tip speed, which is three orders of magnitude smaller than the $0.01\,V_{tip}$ potential aerodynamic quiet-zone criterion. The agreement above the rotor disk, together with the close correspondence of the two-dimensional threshold boundaries, supports the use of the FVM model to identify candidate regions of low rotor-induced velocity and potential aerodynamic quiet-zones for sensor placement.

### 3.1.2 Multi-rotor validation

In addition to the single-rotor validation of the FVM model with the in-house experimental facility, the induced velocity characteristics predicted by the FVM were compared against the experimental investigation reported in the literature by Wilson et al. (2022). The quad-X configuration from this reference paper (3rd row, Fig. 2) is considered for validation. The rotors are 3-bladed, and measure 0.0762 m (3 in.) in di-

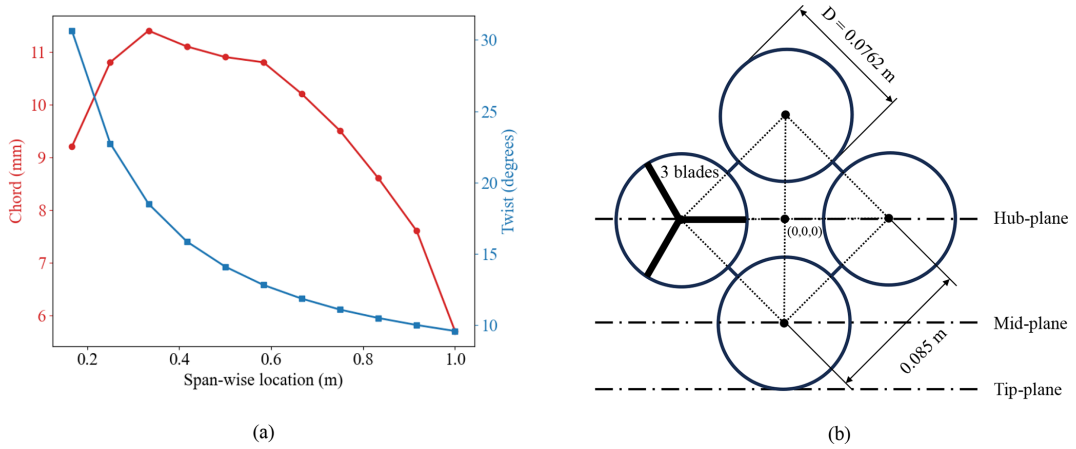


**Figure 10.** Rotor geometry details for the quad-X configuration presented in Wilson et al. (2022).

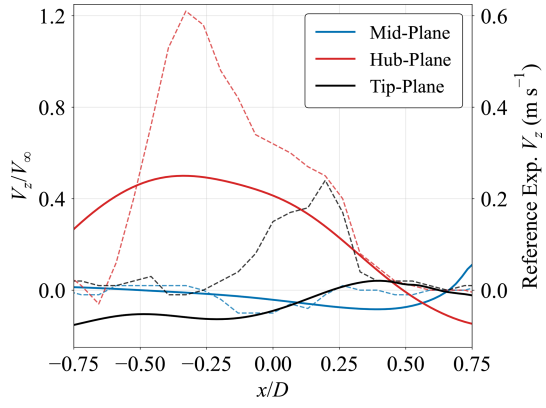


**Figure 11.** Validation of the FVM model for the prediction of vertical component of the velocity field of the quad-X configuration from the reference paper (Wilson et al., 2022).

ameter. No explicit definition of the twist and chord geometry (either in the reference or from the manufacturer) exists to model the rotor geometry in FVM; hence, the chord distribution was measured manually from a digital image using basic scaling formulae, and replicated for the FVM study. Similarly, the rotor was also assumed to be "ideally twisted" (which is a hyperbolic span-wise twist distribution). The measured chord and twist distributions, and other geometric details of the quad-X configuration utilised for the FVM validation are presented in Fig. 10a.

While the original experiments in the reference paper (Wilson et al., 2022) were conducted in a water tunnel, the present FVM validation utilises the equivalent flow conditions in air, obtained by maintaining the same Reynolds Number ($Re = 38\,100$) and advance ratio ($\mu = 0.1393$). Accordingly, the rotor angular speed was set to $\Omega = 1413.7167\,\mathrm{rad\,s^{-1}}$ (225 Hz), and the freestream velocity at $7.5\,\mathrm{m\,s^{-1}}$, consistent with the conditions presented in the reference paper. For the aforementioned geometry and flow parameters, the streamwise variation of the vertical component of the velocity at $Y/D \approx 0.35$ from the rotor disk plane (Fig. 4 in the reference paper) was compared with the FVM predictions for the three measurement planes evaluated in the reference paper, i.e., the hub, mid, and the tip planes (see Fig. 10b).

The obtained velocity profiles are presented in Fig. 11, where, solid curves correspond to FVM predictions, and dashed curves represent the results from the reference paper (Wilson et al., 2022) and the Masters thesis upon which it is based (Brenner, 2021). The induced velocity ($y$-axis) is normalised with the freestream velocity, and the streamwise direction ($x$-axis) is normalised with the rotor diameter ($D$). Additionally, the dimensional values of the original experiments are presented in the secondary $y$-axis. It can be observed from Fig. 11 that the peak velocity at the hub-plane is under-predicted by FVM ($0.5V_\infty$ against $1.25V_\infty$ from the reference results), and so is the peak at the tip-plane. Nevertheless, the location of the minima and maxima are predicted with reasonable accuracy at the various streamwise locations for each of the measurement planes. While the normalised induced velocity trends and order of magnitude are captured by FVM in Fig. 11, lending some confidence in the predictions, visible disagreement in the prediction of exact values exists.

This disagreement between FVM and reference experiments could be attributed to either the assumptions of FVM, or the lack of complete information surrounding the original experimental data. For instance, FVM simulates only isolated rotors, and does not model fuselage and other structural members (out of scope of the present study), whereas complete quad-rotor system is investigated in the reference literature. Furthermore, the values presented in FVM are time-averaged over 10-rotor revolutions after the initial transients have settled. However, details of averaging techniques used to obtain the induced velocity, particle image velocimetry (PIV) measurement uncertainty and accuracy, physical

limitations in resolving the locations of the measurement planes, the associated blockage effects, influence of ambient conditions, and rotor blade geometry (such as airfoil sections, span-wise chord, and twist distributions) are unclear in the reference paper. These quantities influence the induced velocity distribution significantly, and remain essential for effective modelling into FVM. Especially, since the velocities in the reference experiments are not more than $0.6\,\mathrm{m\,s^{-1}}$, without clarity on background flow and the associated measurement uncertainties, it becomes considerably hard to replicate the results and quantify disagreements in prediction with FVM. To identify test cases with more complete information, a detailed review of the literature on wind speed measurements using UAV-mounted sensors was also conducted (Thielicke et al., 2021; Wilson et al., 2022; Ghirardelli et al., 2023; Jin et al., 2024; Ghirardelli et al., 2025). Nonetheless, the reviewed studies exhibited a similar lack of clarity regarding the governing parameters listed above.

In summary, both the single-rotor and multi-rotor validation of the FVM induced velocity predictions illustrate reasonable agreement with the in-house experimental results as well as the reference study. These consistent validations reinforce the capability of the FVM model to predict the induced velocity characteristics of different rotor systems and flow conditions.

### 3.2 Single-rotor system

The focus of this section is on identifying potential aerodynamic quiet-zones around a simple single-rotor system in various flight conditions, which in turn will form the basis for understanding quad and hexa-rotor systems.

The APC $12 \times 6$E single-rotor is considered, and the velocity induced by this rotor is calculated on an equispaced $100 \times 100$ Cartesian grid on the $x$–$z$ plane at $y/R = 0$. The plane extends from $-3.5R$ to $3.5R$ along the $x$-axis and from $-3.0R$ to $10.0R$ along the $z$-axis (see Fig. 4b), where $R$ is the radius of the rotor. The rotor's hub is located at $(0, 0, 0)$, with the rotor disk in the $x$–$y$ plane. All studies were performed at two thrust conditions corresponding to $\mathrm{DL} = 100$ and $300\,\mathrm{N\,m^{-2}}$. Results are presented considering the final ten rotor revolutions, once the numerical transients in the solution and the rotor wake are allowed to settle.

For the single-rotor analysis, three flight conditions are considered: pure hover, axial descent, and forward-flight descent. Hover represents a baseline condition and perhaps one that is most critical for collecting in situ meteorological data at a chosen altitude. In axial descent and forward descent, wake re-ingestion and strong non-uniformities of flow occur above the rotor plane, and sensor placement is very sensitive to these disturbances. In an axial climb scenario, the rotor wake is convected below the rotor disk, and therefore, does not induce much velocity above the plane of the rotor. Consequently, axial climb flight conditions are not presented in this paper for the sake of brevity, as they are not the limiting cases that determine the wind sensor placement location. The non-dimensional parameters defining the flight condition of the rotor are divided into the forward velocity and the axial velocity, defined as $\mu_x = V_{\mathrm{forward}}/V_{\mathrm{tip}}$ and $\mu_z = V_{\mathrm{axial}}/V_{\mathrm{tip}}$, with positive $\mu_z$ denoting axial descent, where the rotor tip speed is given by $V_{\mathrm{tip}} = \Omega R$.

Figure 12 shows the time-averaged wake geometry overlaid on the associated velocity field for three representative flight conditions: hover, axial descent, and forward descent; shown alongside is a binary contour plot for each flight condition, which differentiates the flow field into two regions based on a 1 % tip speed threshold for induced velocity. The binary plots indicate the potential aerodynamic quiet-zones in the flow field, i.e., regions where the rotor wake influences are negligible, hence defining the candidate sensor placement locations for the corresponding flight conditions. For each flight condition in Fig. 12, the left panel presents time-averaged streamlines of the total velocity field in the $x$–$z$ plane alongside the time-averaged wake geometry. Here, total velocity is defined as the superposition of the wake-induced velocity and the prescribed freestream velocity ($\boldsymbol{V}_{\mathrm{tot}} = \boldsymbol{V}_{\mathrm{ind}} + \boldsymbol{V}_{\infty}$). The velocities ($|\boldsymbol{V}_{\mathrm{tot}}| = V_{\mathrm{tot}}$ and $|\boldsymbol{V}_{\mathrm{ind}}| = V_{\mathrm{ind}}$) are normalised by the rotor tip speed ($V_{\mathrm{tip}}$). The rotor blades are denoted by thick, horizontal line segments at $z/R = 0$, and the $x$ and $z$ axes are non-dimensionalised by the rotor radius $R$ to ensure generality across scales. The right panel shows the binary plot, differentiated by shaded regions in red and blue, and otherwise – the shaded portion in darker red denotes the regions dominated by the rotor wake, where the time-averaged induced velocity exceeds 1 % of the blade-tip speed at $\mathrm{DL} = 100\,\mathrm{N\,m^{-2}}$; the lighter red portion denotes the corresponding regions at $\mathrm{DL} = 300\,\mathrm{N\,m^{-2}}$; and regions outside the red-shaded region represent the quiet-zones for the corresponding DL, where the induced velocity is less than 1 % of the blade-tip speed. Shown on these binary plots are also the sensor-accuracy boundaries (which for the TriSonica Mini sensor is $0.2\,\mathrm{m\,s^{-1}}$) for both the operating thrust conditions: darker blue region corresponds to $\mathrm{DL} = 100\,\mathrm{N\,m^{-2}}$ while the lighter blue region represents $\mathrm{DL} = 300\,\mathrm{N\,m^{-2}}$. Across all cases shown in Fig. 12, the induced velocity does not include the freestream component of the total velocity, and therefore the expectation is that the wind sensor should be placed in regions where the induced velocity goes to zero, or correspondingly the sensory-accuracy limitation, so that only the true freestream velocity is measured within the practical threshold limits governed by the choice of the wind speed sensor.

The left panel of Fig. 12a illustrates the wake structure and flow field characteristics of the single-rotor in hover ($\mu_x = 0.00,\ \mu_z = 0.00$). The time-averaged streamlines of the total velocity field indicate that the flow above the rotor disk remains largely vertical and weakly disturbed, while strong velocity gradients are confined primarily to regions below the rotor plane. The right panel provides a more detailed representation of this behaviour; it can be

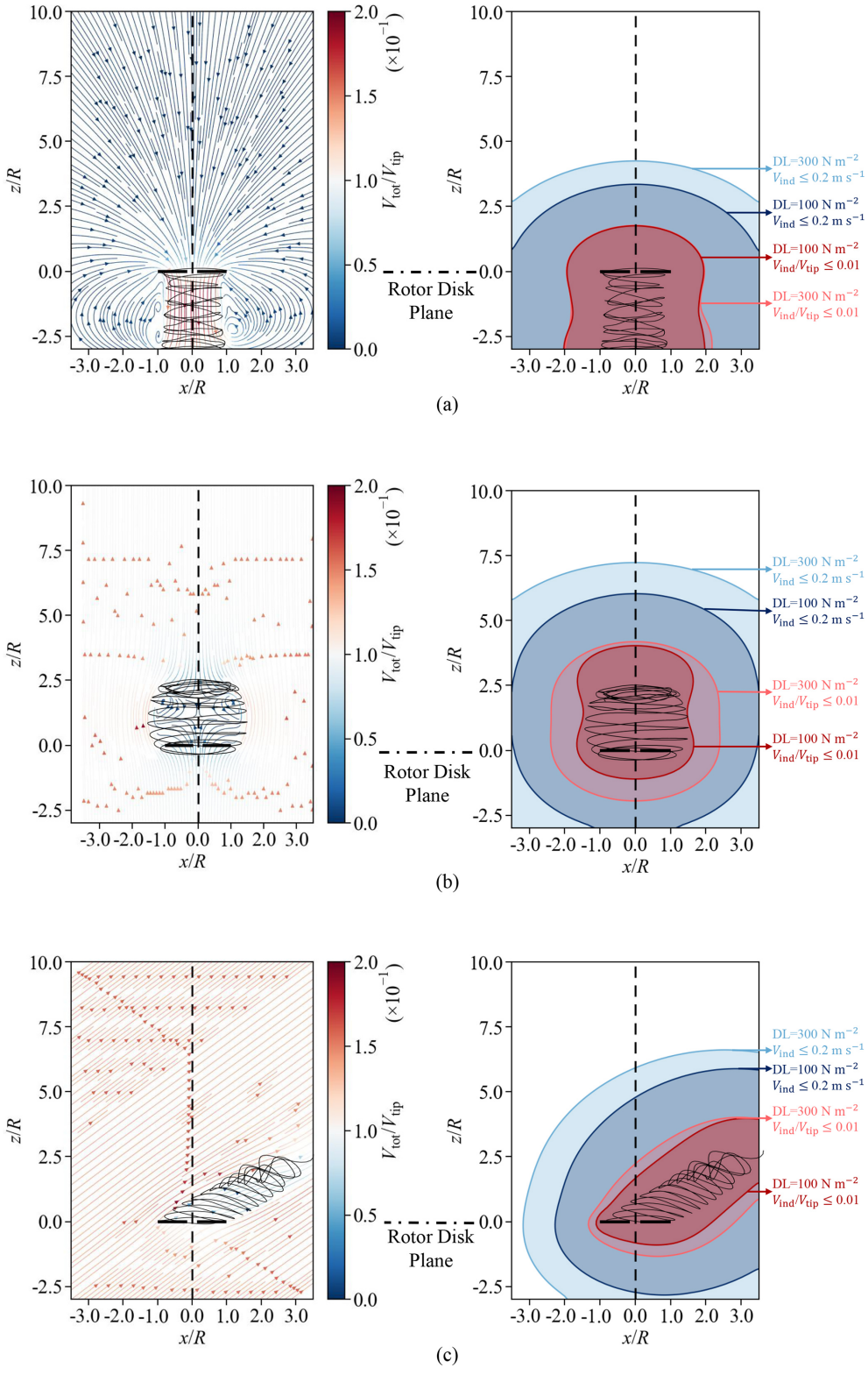


**Figure 12.** Flow field and wake characteristics for the APC single-rotor at DL = 300 N m$^{-2}$: **(a)** hover ($\mu_x = 0.00$, $\mu_z = 0.00$); **(b)** axial descent ($\mu_x = 0.00$, $\mu_z = 0.10$); **(c)** forward descent ($\mu_x = 0.10$, $\mu_z = 0.10$). Quiet-zones are identified based on the 1 % blade-tip speed threshold for induced velocity and the 0.2 m s$^{-1}$ sensor-accuracy boundary at DL = 100 N m$^{-2}$ and DL = 300 N m$^{-2}$.

observed for DL = 300 N m$^{-2}$, represented by the lighter red region for the $V_{ind}/V_{tip} > 0.01$ threshold and lighter blue region for the sensor-accuracy boundary (0.2 m s$^{-1}$) are larger compared to the corresponding darker red and blue regions for DL = 100 N m$^{-2}$. The 1 % tip speed threshold for DL = 100 N m$^{-2}$ (dark red) remains bounded to the vicinity of the rotor disk, approximately spanning $z/R \in (-3, 1.8)$ and $x/R \in (-2, 2)$, while the lighter red region for DL = 300 N m$^{-2}$ spans a similar region, with notable escalations towards the boundary from the lower DL case. The same trend is reflected with the sensor-accuracy boundary, computed based on the specifications of the TriSonica Mini sensor. The potential quiet-zone region ($V_{ind}/V_{tip} \leq 0.01$) occupies a wide area above the rotor plane for $z/R \gtrsim 1.8$ in the case of the smaller DL, and $z/R \gtrsim 1.8$ in the case of the larger DL, suggesting that hover conditions provide a clearly defined region above the rotor plane with minimal wake influence, suitable for wind sensor placement.

Figure 12b presents the corresponding results for a representative axial descent case ($\mu_x = 0.00$, $\mu_z = 0.10$). The maximum tip speed normalised axial or forward velocity considered in the present study ($\mu_{x,z} = 0.2$) corresponds to $\approx 27$ m s$^{-1}$ for the APC 12 × 6E rotor operating at a disk loading of DL = 300 N m$^{-2}$ (the rotor tip speed here is $V_{tip} \approx 135$ m s$^{-1}$). These values reflect real-world flight velocity ranges for UAVs of similar geometrical scale, and are representative of typical operations for meteorological applications. In Fig. 12b, the wake convects upward through the rotor disk in this regime, a feature evident in the left panel and consistent with the classical vortex-ring-state behaviour (Leishman et al., 2002). This upward wake displacement is also apparent with the time-averaged total velocity streamlines, where strong flow distortion both above and below the rotor plane can be observed. The right panel confirms that for DL = 300 N m$^{-2}$, the light red-shaded region ($V_{ind}/V_{tip} > 0.01$) now extends symmetrically across the rotor disk, covering $\approx z/R \in (-2, 3.7)$ over the lateral extent $x/R \in (-2, 2)$ of the plane considered for the calculation of the induced velocity. The darker red region corresponding to DL = 100 N m$^{-2}$ remains confined to a considerably smaller region closer to the rotor disk; consequently, the DL = 300 N m$^{-2}$ case can be regarded as the governing scenario when defining the potential quiet-zone limits for sensor placement. The corresponding quiet-zones for each DL, identified as the exterior region of the shaded red regions, is significantly reduced and confined to regions far from the rotor disk, indicating that under axial descent conditions, most locations above the UAV are strongly influenced by the rotor wake. The minimum $z/R$ required to match the sensor uncertainty stretches to at least $-2.5R$ and $5R$ across the rotor disk, highlighting that axial descent offers only limited regions, located far from the vehicle, where wind sensor placement would experience minimal wake contamination. Accurate wind estimation with a dedicated sensor in these flight conditions is not feasible in realistic conditions owing to such large distances of the potential quiet-zones from the rotor disk.

For a forward descent case ($\mu_x = 0.10$, $\mu_z = 0.10$), the wake and flow field characteristics (shown in Fig. 12c along with the binary plot) reveal several interesting patterns. In this combined inflow condition (axial descent and forward flight), the left panel shows that the tip vortices are deflected downstream, forming an inclined and asymmetric wake structure. This skewing is clearly reflected by the total velocity streamlines, indicating that wake-induced disturbances are advected away from the rotor disk in the direction of flight, leading to reduced velocity gradients upstream of the vehicle. The right panel reveals a pronounced asymmetry in the distribution of wake influence: the lighter red region at DL = 300 N m$^{-2}$ is confined to $x/R = -1$ in the rotor upstream, while stretching beyond the computational domain in the downstream region. The darker red-shaded region corresponding to DL = 100 N m$^{-2}$ remains completely enclosed within the larger DL boundary, indicating a comparatively reduced spatial extent of wake influence at lower DL. Quantitatively, the potential quiet-zones identified as the region outside these shaded red regions, where $V_{ind}/V_{tip} < 0.01$ is observed for $z/R \gtrsim 2.50$ at $x/R = 0$ – this $z/R$ is smaller compared to pure axial descent, but greater than the $z/R$ observed for hover. Upstream locations for forward descent, characterised by negative $x/R$, offer comparatively lower $z/R$ for sensor placement, as low as $\approx 1.25R$ for the larger DL case. This asymmetric quiet-zone bounds is the net effect of both forward motion and wake inclination; and its location is determined by the skew angle of the wake, which is defined as the inclination of the wake relative to the rotor axis ($x$). Nonetheless, the sensor-accuracy boundary (lighter and darker blue-shaded regions in Fig. 12) reveal that the extent of the practically viable quiet-zones can stretch to $\approx 5R$ across the computational domain, severely restricting the options for sensor placement across the planform of the rotor. Therefore, the suitability of these asymmetric axial locations for wind sensor mounting has to be further investigated for different forward descent flight regimes (different $\mu_x$, $\mu_z$) to reach a robust conclusion about the feasibility of utilising a wind speed sensor for wind measurements in these flight regimes.

In general, these findings illustrate that the size and accessibility of wake-quiet regions are significantly dependent on flight conditions. In hover, a symmetric vertically separated aerodynamic quiet-zone exists above the rotor disk. Axial descent eliminates wake-free zones in the vicinity of the UAV, mostly above the rotor disk, while forward flight creates an asymmetric yet accessible quiet-zone positioned upstream of the rotor, but requires detailed investigation of the wake skewness to ascertain candidate locations for sensor placement.

### 3.2.1 Induced velocity distribution at different radial stations

Figure 13 presents the variation of the time-averaged induced velocity ($V_{\text{ind}}$) along the rotor-$z$-axis for three radial (blade span-wise) locations ($r/R = 0, \pm 1$, presented in black, blue, and red colours, respectively, as shown in Fig. 13a). The induced velocity is normalised by $V_{\text{tip}}$, while the rotational axis of the rotor is normalised by its radius ($R$). The shaded bands represent the standard deviation of the induced velocity, corresponding to a $1\sigma$ variation about the mean, evaluated over the final ten rotor revolutions of the converged solution. The mean and standard deviation together represent the temporal variability of the induced flow.

For hover (Fig. 13b), at the rotor hub plane ($r/R = 0$), the time-averaged induced velocity values are negligible upstream of the rotor disk ($z/R > 1.8$). A pronounced peak can, however, be observed immediately downstream ($z/R \approx -1$) of the rotor disk plane, associated with wake contraction; the peak gradually decays farther downstream as the wake expands and diffuses in space, indicating that the region below the rotor ($z/R < -1$) is unsuitable for wind speed measurements. A similar aerodynamically dirty downstream region can be observed for the other radial locations ($r/R = \pm 1$), owing to tip-vortex shedding, and strong wake interactions. The induced velocity values upstream of the rotor disk still remain negligible for practical sensor placement considerations. In axial descent (Fig. 13c), elevated induced velocities persist both above and below the rotor disk plane over a wide axial extent, $z/R \in (-2.50, 4.3)$, reflecting the upward convection of the wake through the disk; although an apparent decay is observed for $z/R \gtrsim 4.3$, this behaviour is partly attributed to truncation of the helical wake in the numerical solution, and in practice all regions above the rotor remain affected by rotor-induced flow. In forward descent flight (Fig. 13d), the upstream induced velocity distribution becomes strongly dependent on radial position and direction as a consequence of the skewed wake geometry, with potential quiet-zones occurring at substantially lower $z/R$ above the rotor plane on the retreating side ($r/R = -1$) compared to the advancing side ($r/R = +1$). Overall, these results demonstrate that potential sensor placement regions are highly dependent on flight condition, with viable low-disturbance zones emerging only when wake inclination (wake skew angle) displaces rotor-induced flow away from the measurement location.

### 3.2.2 Minimum quiet-zone distances across flight conditions

To attain a comprehensive understanding of the influence of the flight condition on the potential quiet-zones for wind-sensor placement, various combinations of axial and forward speeds are studied in detail. Figure 14 presents the minimum axial distance of the quiet-zone from the rotor disk, normalised by the rotor radius ($(z/R)_{\text{min}}$) for four different descent conditions ($\mu_z = 0.05$, 0.10, 0.15, 0.20). The quiet-zone is delineated using the 1 % tip speed threshold (as in the calculations utilised to obtain the right panel of Fig. 12). For each descent case, the minimum quiet-zone distance $(z/R)_{\text{min}}$ was obtained for various forward flight speeds given by advance ratio $\mu_x = 0.00$, 0.05, 0.10, 0.15, 0.20, where $\mu_x = 0.0$ is pure descent, and the other cases correspond to various forward descent conditions. Two DL values (100 and 300 $\text{N m}^{-2}$) are presented in each case. Additionally, a schematic showing the minimal axial distance on the single-rotor is also presented; in the interest of brevity, only the hub plane ($r/R = 0$) results are detailed here.

For the weak axial descent case ($\mu_z = 0.05$, Fig. 14b), $(z/R)_{\text{min}}$ initially increases with $\mu_x$, reaching a maximum around $\mu_x = 0.05$, 0.10 for the low and high DL cases, respectively, before decreasing as $\mu_x$ increases further (this non-monotonic behaviour arises from a transition between a predominantly axisymmetric wake at low $\mu_x$) and a progressively skewed wake at higher $\mu_x$, where downstream convection brings the low-disturbance region closer to the rotor plane. In the moderate axial descent case ($\mu_z = 0.10$, Fig. 14c), $(z/R)_{\text{min}}$ decreases with increasing $\mu_x$ for the lower DL case. The higher DL case demonstrates the decrease in $(z/R)_{\text{min}}$ up to $\mu_x \approx 0.10$, followed by a brief increase peaking around $\mu_x = 0.15$, before decreasing again at higher $\mu_x$. This behaviour reflects competing effects between wake skewing, which generally lowers $(z/R)_{\text{min}}$, and localised wake thickening caused by the interaction of axial inflow with edgewise motion.

For stronger axial descent conditions ($\mu_z = 0.15$) and $\mu_z = 0.20$ (Fig. 14d and e), $(z/R)_{\text{min}}$ decreases more consistently with increasing $\mu_x$, a trend that is most clearly observed for the higher disk loading case DL = 300 $\text{N m}^{-2}$ (under strong axial inflow, the wake remains more coherent and aligned with the rotor axis, and increasing edgewise motion primarily skews the wake away from the rotor-hub axis, reducing the axial extent of the disturbed region). In contrast, except for the $\mu_z = 0.05$ case, the lower disk loading condition (DL = 100 $\text{N m}^{-2}$) exhibits a consistently monotonic decrease of $(z/R)_{\text{min}}$ with $\mu_x$ for a given $\mu_z$ (weaker induced velocities result in a more rapidly convected wake, limiting upstream disturbance).

Across both DL cases, $(z/R)_{\text{min}}$ generally increases with increasing magnitude of axial descent $\mu_z$ for a fixed $\mu_x$ (because stronger axial inflow intensifies the induced velocity field and displaces the disturbed wake region farther upstream). Notably, for pure axial descent conditions with $\mu_x = 0.0$, the values of $(z/R)_{\text{min}}$ for DL = 100 and 300 $\text{N m}^{-2}$ are nearly identical (since in the absence of edgewise motion, wake symmetry dominates and DL primarily scales velocity magnitude rather than wake topology). The hover condition ($\mu_x = 0.0$, $\mu_z = 0.0$) is not included as part of this analysis to emphasise the non-hover flight regimes, where wake asymmetry and axial inflow effects sig-

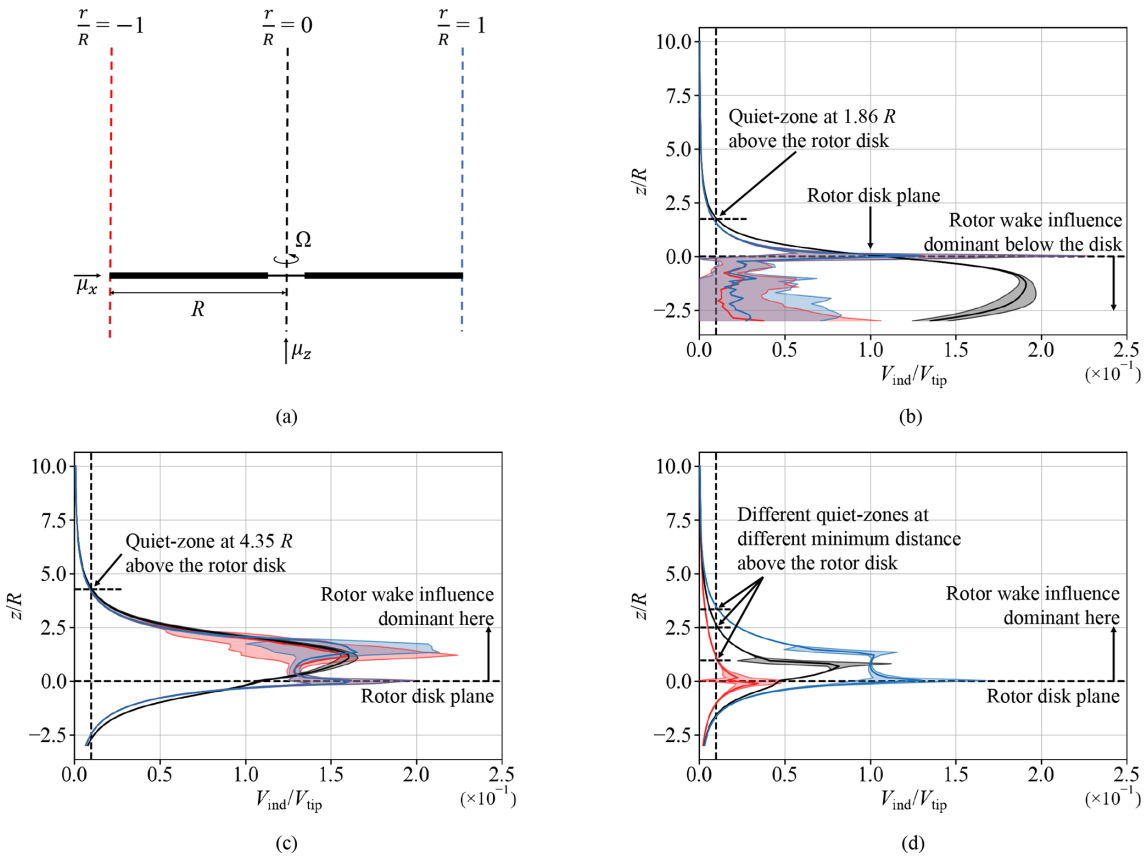


**Figure 13.** Axial variation of induced velocity for the APC single-rotor at various span-wise locations: **(a)** span-wise locations considered for induced velocity analysis; **(b)** hover ($\mu_x = 0.00$, $\mu_z = 0.00$); **(c)** axial descent ($\mu_x = 0.00$, $\mu_z = 0.10$); **(d)** forward descent ($\mu_x = 0.10$, $\mu_z = 0.10$), all at DL = 300 N m$^{-2}$.

nificantly influence sensor placement. Overall, these results indicate that potential wind speed sensor placement requires the greatest axial separation under pure axial descent and weak forward descent scenarios, while higher forward descent conditions permit sensor placement closer to the rotor hub plane compared to pure axial descent, with higher DL consistently increasing the required clearance.

### 3.3 Multi-rotor systems

The single-rotor analysis is extended to quad-rotor and hexa-rotor configurations, to ensure applicability to practical configurations in the UAV space, where such multi-rotor systems are the predominant design choice. The APC propeller (refer Table 1 for the geometry data) is considered for both the multi-rotor configurations, and the time-averaged total velocity streamlines, along with the quiet-zone binary plots are presented at different $x$–$z$ planes passing through different regions of the rotor system. All multi-rotor numerical simulations are carried out with an identical initial azimuth of 0° (Southward if viewed from top) for each rotor. Since the numerical framework prescribes a constant rotational speed ($\Omega$), the relative phase angle between the blades of the rotors remain perfectly locked throughout the simulation. The multi-rotor systems considered in the present study feature non-overlapping rotor disks. Therefore, the total disk loading is

$$\mathrm{DL} = \frac{N_\mathrm{r} T}{N_\mathrm{r} A} = \frac{T}{A}.$$

(where $N_\mathrm{r}$ is the number of rotors, $T$ is the thrust produced by each rotor, and $A$ is the corresponding disk area) is equal to the disk loading of the individual rotors. The rotational speed of the rotors are fixed (according to the experimental validation of performance curves with the manufacturer) to produce the desired thrust, and therefore, each rotor and the consequently, the entire system operate at the same disk loading. Only the hovering flight condition is discussed in this section for the following reasons:

1. One of the primary meteorological requirements for wind speed measurements is the capability of collecting data over a sustained period of time at any given location. Hovering VTOL multi-rotor systems allow for point measurements in space over a long period, satisfying this exact requirement, consequently illustrating the

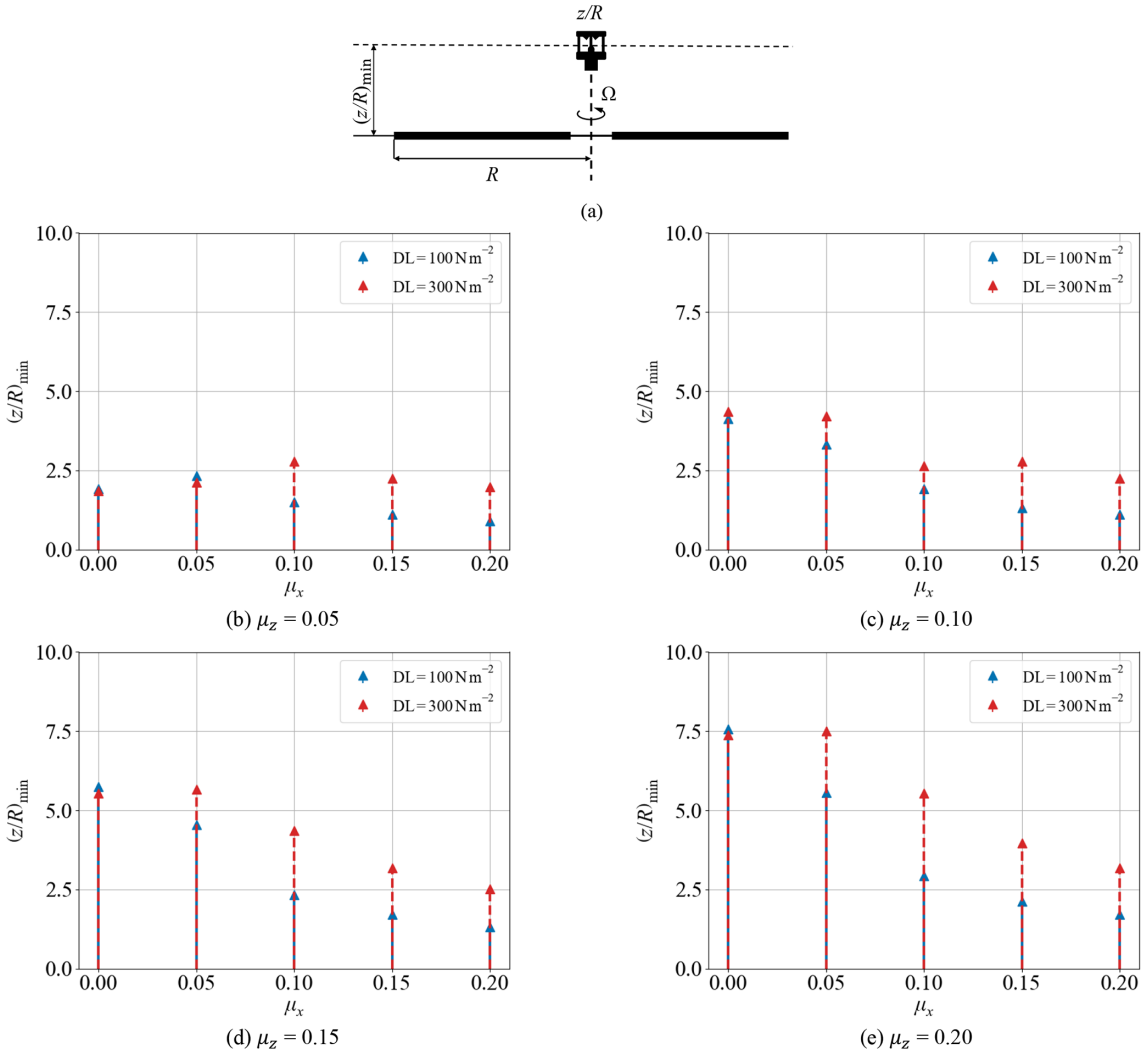


**Figure 14.** Variation of the minimum axial location of the quiet-zone at the rotor hub for the APC single-rotor: **(a)** schematic representation of the definition of $(z/R)_{\min}$; **(b)** $\mu_z = 0.05$; **(c)** $\mu_z = 0.10$; **(d)** $\mu_z = 0.15$; **(e)** $\mu_z = 0.20$.

importance of hovering flight for effective wind speed measurements.

2. Similar to the results observed with the single-rotor system, a descending flight condition will cause the rotor wake to be convected up through the rotor disk, and will interfere with the sensor signals. A similar argument can be made for descending forward flight conditions, given the highly prevalent rotor-rotor and rotor-wake interactions in these multi-rotor systems. Therefore, emphasis is placed primarily on "hover" as the critical flight condition for UAV-based wind speed measurements.

### 3.3.1 Quad-rotor

Figure 15a shows the configuration of the APC quad-rotor system considered in the study. The rotor disk is positioned along the $x$–$y$ plane with inter-rotor spacings chosen appropriately based on existing UAVs. For the induced velocity computations, two equispaced $100 \times 100$ Cartesian grids in the $x$–$z$ plane are chosen; (a) Plane I, passing through the geometric centre of the system (GC) at $(0, 0, 0)$, and (b) Plane II, passing through the hubs of rotors 1 $(-1.05R, 1.05R, 0)$ and 4 $(1.05R, 1.05R, 0)$, respectively, as shown in Fig. 15b. The wake from each rotor is split into blue and red colour, to highlight the blade from which these vortices are trailed. Compared to a single-rotor wake, the structure beneath the quad-rotor is more complex, owing to significant rotor-rotor interactions. The target planes for induced velocity computations extend from $-3.5R$ to $3.5R$ along the $x$-axis and from $-3.0R$ to $10.0R$ along the $z$-axis. All investigations are conducted on a DL of $100\,\mathrm{N\,m^{-2}}$ and $300\,\mathrm{N\,m^{-2}}$, and similarly to the case of the single-rotor, results are reported over the final ten rotor revolutions, after the numerical transients in the solution are allowed to settle.

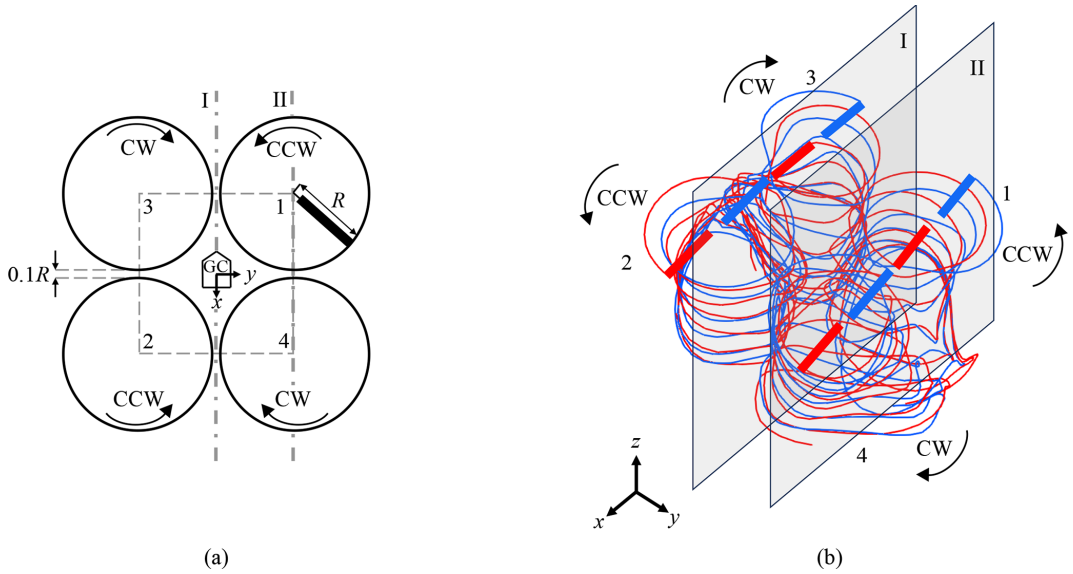


**Figure 15.** Quad-rotor configuration and corresponding time-averaged wake trajectories: **(a)** quad-rotor configuration utilised in the present study; **(b)** isometric view of the calculated time-averaged wake trajectories of all rotors in the quad-rotor configuration.

Figure 16 illustrates the flow field characteristics of the quad-rotor system in hover, on the two planes shown in Fig. 15. The panels on the left present the total velocity streamlines normalised by $V_{\text{tip}}$, while the right panels represent the potential quiet-zones identified using the 1 % blade-tip speed threshold for the induced velocity. The darker red and blue shaded regions correspond to the locations where the magnitude of the induced velocity satisfies $V_{\text{ind}}/V_{\text{tip}} > 0.01$, and the corresponding sensor-accuracy boundary of $0.2\,\text{m}\,\text{s}^{-1}$ respectively, for $\text{DL} = 100\,\text{N}\,\text{m}^{-2}$. The lighter shades of red and blue depict the same regions for $\text{DL} = 300\,\text{N}\,\text{m}^{-2}$. Regions outside these red-shaded regions are defined as the potential aerodynamic quiet-zones, while the blue regions denote the overall sensor-accuracy boundary achieved based on the operating thrust condition. As expected, if the DL is higher, the sensor has to be placed further away from the rotor disk plane compared to if the DL is lower.

Figure 16a shows the time-averaged streamlines and the threshold plot for Plane I. The horizontal dashed line segments at $z/R = 0$ indicate the projected blade locations in the $y$-direction, since the rotor disks are not visible in this plane. The flow field below the rotor disk plane is governed by the interaction of the individual rotor wakes, an inherently unsteady process. Although instantaneous structures are highly transient, the time-averaged streamlines on the left panel (Fig. 16a) indicate a complex but organised wake topology, with symmetric recirculation regions formed by the merging rotor-induced vortices. The lighter red region (right panel), corresponding to $\text{DL} = 300\,\text{N}\,\text{m}^{-2}$, extends further above the rotor disk plane, and along the lateral direction ($x/R$) than the darker red region for $\text{DL} = 100\,\text{N}\,\text{m}^{-2}$. This indicates that increased disk loading primarily enlarges the wake-dominated region above the rotor plane defined by $V_{\text{ind}}/V_{\text{tip}} > 0.01$. The minimum axial location above the disk plane at the GC that satisfies the induced velocity threshold is $(z/R)_{\text{min}} \approx 3.4$ at the higher disk loading and $\approx 3.2$ at the lower disk loading.

Figure 16b presents the corresponding flow field for Plane II, where the plane intersects the rotor disks of rotors 1 and 4. At the GC, the induced velocity field above the rotor plane is stronger, which may be attributed to the cumulative superposition of the induced velocity components from all four rotors, leading to a locally amplified upward influence in the central region. For Plane II, the regions defined by the 1 % blade-tip speed threshold further highlight this distinction – the potential aerodynamic quiet-zone, defined by $V_{\text{ind}}/V_{\text{tip}} \leq 0.01$ is achieved at a lower axial location for Plane II, with $(z/R)_{\text{min}} \approx 3.2$, compared to $(z/R)_{\text{min}} \approx 3.4$ at the GC, for a similar lateral extent of $x/R \in (-3.5, 3.5)$ at $\text{DL} = 100\,\text{N}\,\text{m}^{-2}$. Assuming geometric symmetry in hover, a plane passing through the hubs of rotors 2 and 3 may be expected to exhibit behaviour similar to Plane II. Therefore, under hover and axial climb conditions, where wake development is predominantly directed below the rotor disks, a plane such as Plane II offers a comparatively cleaner location for wind sensor placement than the GC, owing to the earlier attainment of the quiet-zone above the rotor plane.

It is noted, however, that the difference in axial extent between the two configurations is relatively small, and if structural or airframe constraints and stability requirements limit sensor placement toward the GC instead of the locations such as Plane II, the GC may still be considered a viable mounting location, as the increase in the minimum threshold height

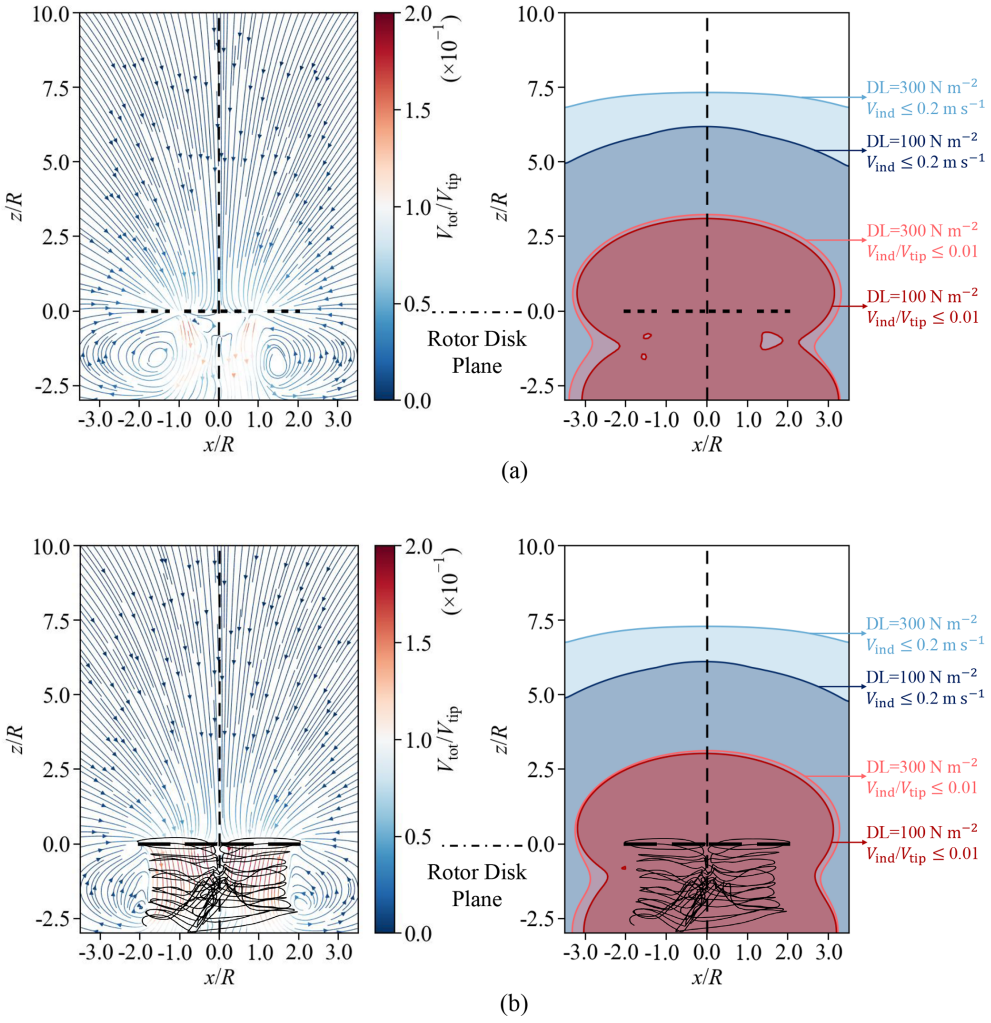


**Figure 16.** Flow field and wake characteristics for the APC quad-rotor in hover at DL = 300 N m$^{-2}$: **(a)** $x$–$z$ plane passing through the geometric centre (Plane I); **(b)** $x$–$z$ plane passing through the hubs of rotors 1 and 4 (Plane II). Quiet-zones are identified using the 1 % blade-tip speed threshold for induced velocity and the 0.2 m s$^{-1}$ sensor-accuracy boundary for DL = 100 N m$^{-2}$ and DL = 300 N m$^{-2}$.

remains modest. While the 1 % tip speed threshold provides $z/R \in [3.2, 3.4]$ for the cases presented, due consideration should be given to the sensor-accuracy limits (based on the sensor utilised) – in the present study, the TriSonica Mini sensor uncertainty of 0.2 m s$^{-1}$ pushes the boundary of minimum axial location for candidate sensor placement locations to significantly large $z/R$ values, stretching at least $6R$ from the rotor disk plane. However, these locations do not offer any practical advantages compared to the reported range of axial locations, i.e. $z/R \in [3.2, 3.4]$ obtained based on the 1 % tip speed threshold, since the lowest possible resolution of the sensor is already achieved in the aforementioned candidate locations.

### 3.3.2 Hexa-rotor

A hexa-rotor configuration of the APC rotor is shown in Fig. 17a, where the rotor disk is positioned along the $x$–$y$ plane. For the induced velocity computations, three equispaced $100 \times 100$ Cartesian grid in the $x$–$z$, and $y$–$z$ planes are chosen – Plane I, passing through the system GC at $(0, 0, 0)$, Plane II, passing through the hubs of rotor 3 $(1.82R, -1.05R, 0)$ and 5 $(1.82R, 1.05R, 0)$, and Plane III, passing through the hubs of rotor 4 $(-1.82R, 1.05R, 0)$ and 5 $(1.82R, 1.05R, 0)$. The target planes extend $-3.5R$ to $3.5R$ along the $x$ and $y$-axis, and from $-3.0R$ to $10.0R$ along the $z$-axis. All investigations are performed at a DL of 100 N m$^{-2}$ and 300 N m$^{-2}$, and results are presented over the final ten rotor revolutions of the simulation, after transients in the solution are allowed to settle. Illustrations are similar to the quad-rotor system – the time-averaged streamlines and the potential quiet-zone estimation are detailed for three planes (Planes I, II, and III) shown in Fig. 17.

The flow field characteristics of the hexa-rotor in hover, are shown in Fig. 18 for the three planes, I–III. Similar to the

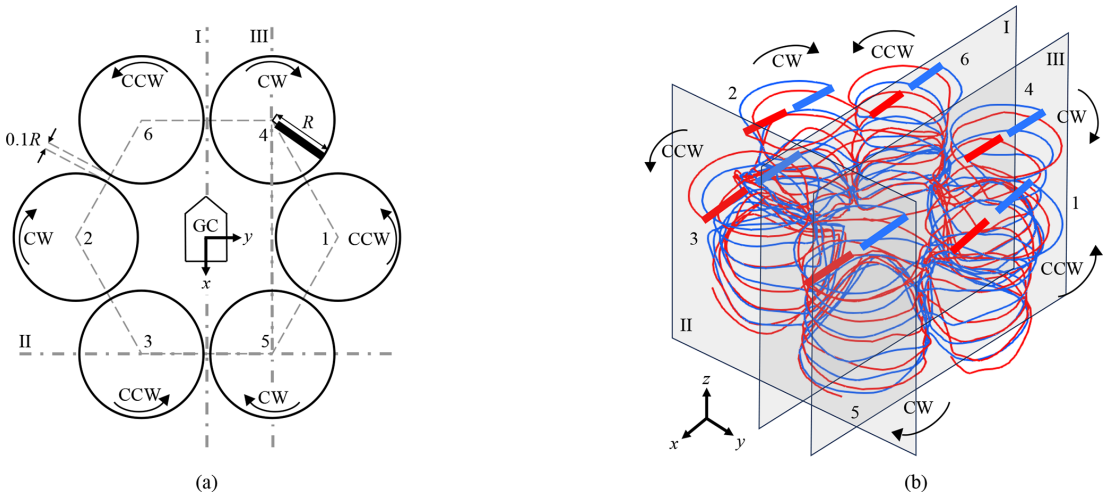


**Figure 17.** Hexa-rotor configuration and corresponding time-averaged wake trajectories: **(a)** Hexa-rotor configuration utilised in the present study; **(b)** Isometric view of the calculated time-averaged wake trajectories of all rotors in the configuration.

quad-rotor results, the panels on the left of Fig. 18 depict the time-averaged total velocity streamlines, and the right panels illustrate the binary plots of potential quiet-zones for sensor placement, based on the 1 % tip speed threshold for the induced velocity. The darker red regions indicate areas where the time-averaged induced velocity exceeds the specified threshold for $\mathrm{DL} = 100\,\mathrm{N\,m^{-2}}$, whereas the lighter red regions denote the corresponding regions for $\mathrm{DL} = 300\,\mathrm{N\,m^{-2}}$.

At Plane I (refer to Fig. 17), the time-averaged streamlines on the left panel reveal a considerably asymmetric flow field beneath the rotor system. In practice, these wake structures are aperiodic, which may be the reason for the lack of a symmetric structure even in the time-averaged characteristics. Since none of the rotor disks intersects this plane, the dashed horizontal line segments at $z/R = 0$ denote the projection of the rotor blades in the $y$-direction, representing the plane of the rotor disk. Higher magnitudes of the induced velocity extend laterally beyond the projected rotor disks along $x/R$, indicating pronounced cross-rotor wake interactions near the system GC. The binary plot in the right panel of Fig. 18a identifies regions where the time-averaged induced velocity exceeds the 1 % blade-tip speed threshold. In the vicinity of the GC and within $x/R \in (-1.0, 1.0)$, the total velocity below the rotor disk is directed upward and briefly crosses the rotor plane, persisting up to approximately $z/R \approx 0.27$. Immediately above this location, for $z/R \gtrsim 0.27$, the velocity reverses direction, consistent with the normal inflow direction above a hovering rotor. The opposing contributions near this axial location result in a local reduction of the magnitude of the induced velocity, leading to a narrow quiet-zone window for both the operating thrust conditions, i.e., $\mathrm{DL} = 100$ and $300\,\mathrm{N\,m^{-2}}$. However, this cancellation is confined to a limited axial extent. Beyond this brief window, the cumulative induced field from the six rotors dominates, leading to $V_{\mathrm{ind}}/V_{\mathrm{tip}} > 0.01$ farther above the disk plane. The wake-dominated region extends further upstream for $\mathrm{DL} = 300\,\mathrm{N\,m^{-2}}$ than for $\mathrm{DL} = 100\,\mathrm{N\,m^{-2}}$, reflecting the stronger global induced field associated with higher disk loading. The minimum axial location at which the threshold is satisfied at the GC is $(z/R)_{\mathrm{min}} \approx 3.3$, beyond which a sustained quiet-zone is established. The sensor-accuracy boundary can also be observed to shift beyond the quad-rotor limits, greater than $\approx 7R$ for both the DL values.

Figures 18b and 18c depict the flow field characteristics on planes II and III, respectively. Both planes pass through two rotors each – Plane II, passing through adjacent rotors (3 and 5) separated by $0.1R$ between the rotor tips, and Plane III, passing through rotors (4 and 5), the distance between the tips of the rotors being $\approx 3.6R$. A qualitative analysis of the wake behaviour for both planes II and III reveals that the proximity of the rotors to each other and the surrounding rotors create strong rotor wake interactions downstream of the rotor system, which in turn affect the induced velocity distribution. Such interactions are predominant around $z/R \approx -2$, as can be observed from the left panels of Figs. 18b and c present the time-averaged streamlines for planes passing through rotors 3–5 and 4–5, respectively. The wake interaction below the disks remains strong in both planes, while a localised reduction in the magnitude of the induced velocity is observed along the plane centreline ($x/R = 0$) in Plane III (Fig. 18c). This reduction is primarily influenced by the nearby counter-rotating rotor 1, whose opposing azimuthal velocity component partially offsets the swirl induced by rotors 4 and 5 in the inter-rotor region, thereby decreasing the net induced velocity magnitude along the centreline.

The binary plots (right panels) provide a clearer assessment of the quiet-zone extent. For the plane intersecting rotors 3 and 5 (Fig. 18b), the induced velocity threshold is satisfied at $(z/R)_{\mathrm{min}} \approx 3.1$ for $\mathrm{DL} = 300\,\mathrm{N\,m^{-2}}$. For the plane in-

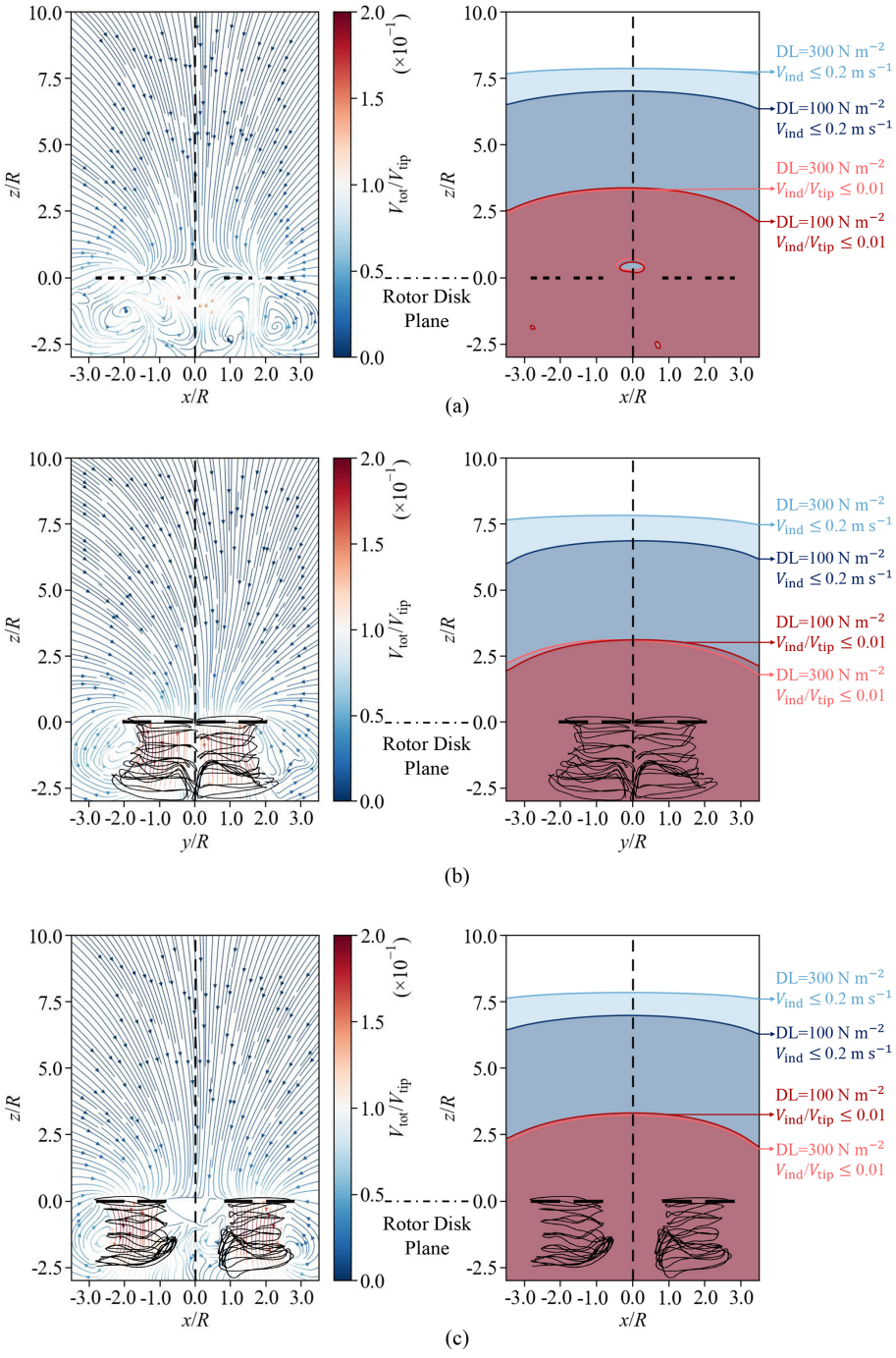


**Figure 18.** Flow field and wake characteristics for the APC hexa-rotor in hover: **(a)** $x$–$z$ plane passing through the geometric centre (Plane I); **(b)** $y$–$z$ plane passing through the hubs of rotors 3 and 5 (Plane II); **(c)** $x$–$z$ plane passing through the hubs of rotors 4 and 5 (Plane III). Results shown at DL = 300 N m$^{-2}$ with corresponding quiet-zone identification based on the 1 % blade-tip speed threshold and the 0.2 m s$^{-1}$ sensor-accuracy boundary for DL = 100 and 300 N m$^{-2}$.

tersecting rotors 4 and 5 (Fig. 18c), the corresponding value is slightly higher, at $(z/R)_{\min} \approx 3.2$ at the same DL. Although a localised reduction in the induced velocity is evident along the centreline in Plane III, a similar feature is not prominently observed in Plane II. However, in both cases, the flow immediately upstream of the individual rotor disks continues to exhibit $V_{\text{ind}}/V_{\text{tip}} > 0.01$, which limits the practical placement of a wind speed sensor near the rotor disk. Comparing these results with the GC configuration, where $(z/R)_{\min} \approx 3.3$, the planes may be ranked in increasing or-

der of minimum quiet-zone height as: Plane II, Plane III, and Plane I (GC). Thus, from a purely aerodynamic standpoint, the plane passing through rotors 3 and 5 (Plane II) offers the most favourable axial location for sensor placement, as it achieves the quiet-zone at the lowest normalised height. Nevertheless, practical integration constraints must also be considered. The structural layout or components of the airframe may restrict asymmetric placement. The placement at GC may also be preferable, considering the relatively lower variation in the minimum $z/R$ for candidate sensor placement locations across the evaluated planes, similar to the observations of the quad-rotor results. Overall, the planes II or III offer the least aerodynamically quiet axial distance for sensor placement, but the GC can still be considered as an effective location across flight conditions due to symmetry and stability considerations. Therefore, careful coordination between aerodynamic, structural, and flight stability considerations is required to determine the final mounting location.

## 4 Summary and Conclusions

Current atmosphere measurement techniques utilise single-use systems or expensive ground-based instruments, among several other methods. The potential for instrumented vertical take-off and landing Unmanned Aerial Vehicles (VTOL-UAVs) to complement (and in some cases replace) existing techniques is immense, given the higher accessibility, controllability, and resolution of the measurements possible with these systems. A critical decision is the placement of wind speed and other sensors that are sensitive to surrounding flow. To that end, the present study examines the influence of rotor-induced flow on single and multi-rotor systems, with the objective of identifying quantitatively reliable locations, or aerodynamic quiet-zones, devoid of wake effects that are suitable for positioning wind speed measurement (or other) sensors. An in-house, free-vortex wake model (FVM) framework is utilised, and the flow field characteristics of isolated UAV-scale single, quad, and hexa-rotor systems are studied under various flight conditions of hover, axial descent, and forward descent. The rotor systems are operated at a disk loading (DL) of 100 and $300\,\mathrm{N\,m^{-2}}$ to ensure a physically meaningful comparison that is independent of the vehicle scale or configuration. Validation of the FVM model is carried out against in-house experimental velocity measurements and literature studies, to strengthen the credibility of the FVM model in capturing key flow field features. A 1 % tip speed threshold (translates to roughly less than $1\,\mathrm{m\,s^{-1}}$ for most designs) is defined for the induced velocity, to identify potential quiet-zones in a flow field, which subsequently translates into candidate locations for wind-sensor placement. Additionally, arguments on sensory accuracy boundary are also placed alongside the tip speed threshold definitions to better understand the practical limitations in guiding sensor placement on UAVs.

Specific conclusions from the present study are as follows.

1. *Single-rotor system.* It was observed that the extent of the quiet-zones was governed by the flight condition of the vehicle, with hovering flight being the critical condition providing the upper limit of potential quiet-zones.
    a. In hover, the wake is confined to downstream of the rotor disk plane, resulting in symmetric, and well-defined quiet-zones above and to the side of the rotor disk. Immediately above the rotor, the sensor can be placed at a minimum distance of $\approx 1.8R$ based on the defined tip speed threshold, or an according value dictated by sensor-accuracy and stability constraints. As expected, sensor placement below the rotor disk would result in significant flow from the rotor wake. Sensors can also be placed laterally along the plane of the rotor from a minimum distance of $2R$, if required.
    b. In axial descent, there exists no potential sensor placement location upstream or downstream of the rotor disk owing to the complex wake topology surrounding the rotor system across a wide lateral extent. In a practical scenario, there would be no viable location below the rotor due to the presence of a fuselage (out of the scope of this study).
    c. In forward descent, based on the specific flight trajectory, there exist limited aerodynamic quiet-zones above the rotor disk as the wake is convected away from the disk owing to the freestream velocity at a skew angle. Sensor placement can be considered on the basis of specific mission requirements.
2. *Multi-rotor systems.* Flow around the quad-rotor and hexa-rotor configurations is considerably complex owing to rotor-rotor interactions, which results in a wide spatial region around the rotor system where the induced flow is significant. Consequently, potential quiet-zones for sensor placement exist on multiple planes of interest, perpendicular to the rotor disk planes. While the vehicle GC is not the most aerodynamically favourable region compared to other planar locations, the variation in the obtained $z/R_{\mathrm{min}}$ is considerably small across all these locations ($\approx 5\,\%$), thereby motivating the use of GC as candidate locations for sensor placement, considering vehicle geometric symmetry and stability constraints. For both the quad and the hexa-rotor systems together, these potential quiet-zone boundaries exists across planes under conservative limits of $z/R \in [3.1, 3.4]$, with a higher disk loading exhibiting a greater axial separation of the sensor from the rotor disk plane. Under careful consideration of the sensor-accuracy boundaries of the employed wind speed sensor, and these $z/R$ limits for different planar measurement locations, candidate locations for sensor placement could appropriately be derived.

3. By focusing on the primary flow field characteristics of various rotor systems, the present study offers quantitative and qualitative guidance for the placement of sensor for atmospheric measurements on VTOL multirotor systems. The practical choice of sensor location will also be driven by constraints in airframe design and flight stability considerations, alongside the specifications and limitations of the sensor parameters.

## Appendix A: Sources of rotorcraft data used in Fig. 6

The data points in Fig. 6 use manufacturer and official database values. Sources are listed in Table A1, with consistent definitions of maximum take-off weight, rotor area, disk loading, and SI-unit conversions applied throughout.

**Table A1.** Sources of the rotorcraft data used in Fig. 6.

| S. No. | Rotorcraft | Reference |
|---|---|---|
| UAVs | | |
| 1 | Dragonfly C-3XL | Draganfly (2026a) |
| 2 | Dragonfly H-L | Draganfly (2026b) |
| 3 | HZH JY30 | Hongfei Aviation Technology Co., Ltd. (2026a) |
| 4 | HZH Y150 | Hongfei Aviation Technology Co., Ltd. (2026b) |
| 5 | JOUAV CW-20 | sUAS News (2016) |
| 6 | JOUAV CW-25E | JOUAV (2026a) |
| 7 | JOUAV CW-25H | JOUAV (2026b) |
| 8 | JOUAV CW-30E | JOUAV (2026c) |
| 9 | JOUAV CW-80E | JOUAV (2026d) |
| 10 | Meteodrone MM670 | Meteomatics (2026) |
| 11 | MotioNew H100 | MotioNew (2026) |
| 12 | UAVOS | UAVOS (2026) |
| Helicopters | | |
| 13 | AS 332 Puma | |
| 14 | SA 365 Dolphin | |
| 15 | AS 350B Squirrel | |
| 16 | Augusta A109 | |
| 17 | Bell 206 | |
| 18 | Bell 412 | |
| 19 | Bell AH-1 Cobra | |
| 20 | Bell 222B | |
| 21 | Boeing CH-46* | |
| 22 | Boeing CH-47C* | Leishman (2006c) |
| 23 | MBB BO 105 | |
| 24 | MBB BK 117 | |
| 25 | Hughes 500E | |
| 26 | AH-64 Apache | |
| 27 | Robinson R22 | |
| 28 | Schweizer 300 | |
| 29 | Sikorsky UH-60 | |
| 30 | Sikorsky S-76A | |

* Tandem Design.

## Appendix B: Disk loading and cross-scale trends in rotor-induced velocity

Disk loading (DL), defined as the ratio of rotor thrust to the swept disk area, provides a physically meaningful parameter for comparing rotor systems operating at different scales. For an ideal rotor in hover, momentum theory gives the induced velocity at the rotor disk as

$$v_i = \sqrt{\frac{T}{2\rho A}} = \sqrt{\frac{\mathrm{DL}}{2\rho}}, \tag{B1}$$

where $T$ is the rotor thrust, $A$ is the swept disk area, and $\rho$ is the air density. Thus, at a given air density, DL defines a characteristic induced velocity scale and provides a useful basis for comparing rotor systems in hover.

However, equal disk loading does not by itself establish complete aerodynamic similarity. The induced velocity distribution can also depend on rotor geometry, solidity, blade number, and compressibility, among other factors. These effects may be particularly relevant when comparing fixed-pitch, electrically driven UAV rotors, whose thrust is primarily controlled through rotational speed, with larger helicopter rotors, whose thrust is commonly adjusted through collective pitch. Therefore, to examine the extent to which the normalised induced velocity profiles remain comparable at equal disk loading, the influence of blade solidity, number of blades, rotor radius and tip Mach number were studied.

Three rotor systems are considered: the Harrington single-rotor (HSR), representing a full-scale helicopter rotor with radius $R = 3.81$ m (Harrington, 1951); the APC $12 \times 6$E propeller, representing a small-scale UAV rotor with radius $R = 0.15$ m (APC Propellers, 2026); and the Hobbywing 2480 (HW) propeller, representing a medium-scale UAV rotor with radius $R = 0.31$ m (HobbywingDirect, 2026). The comparisons are conducted in hover at a prescribed disk loading of $\mathrm{DL} = 100\,\mathrm{N\,m^{-2}}$. The time-averaged induced velocity is normalised by the corresponding rotor-tip speed, $V_{\mathrm{tip}} = \Omega R$, and evaluated along the normalised rotational axis of the rotor, $z/R$. This non-dimensionalisation permits comparison of the axial profiles across the different rotor scales, while recognising that the parameters may affect their dimensional distributions. The various rotor systems and the corresponding parameters studied for the cross-scale generalisation are listed in Table B1.

**Table B1.** Rotor geometry and flow parameters for the HSR, APC, and HW rotors, along with the minimum axial location for potential quiet-zone $(z/R)_{\mathrm{min}}$, computed at the rotor hub corresponding to the $V_{\mathrm{ind}}/V_{\mathrm{tip}} = 0.01$ threshold. $\mathrm{DL} = 100\,\mathrm{N\,m^{-2}}$ for all rotors, and bold values indicate the baseline parameters. For each rotor, the solidity cases are listed in the order $-10\,\%$, baseline, and $+10\,\%$.

| Parameters | Rotor type | | | | | |
|---|---|---|---|---|---|---|
| | HSR | | APC | | HW | |
| | Value | $(z/R)_{\mathrm{min}}$ | Value | $(z/R)_{\mathrm{min}}$ | Value | $(z/R)_{\mathrm{min}}$ |
| Rotor radius, $R$ (m) | 3.81 | – | 0.15 | – | 0.31 | – |
| Solidity, $\sigma$ | 0.069 | 1.929 | 0.079 | 1.684 | 0.063 | 1.181 |
| | **0.076** | 1.924 | **0.088** | 1.737 | **0.070** | 1.197 |
| | 0.084 | 1.926 | 0.097 | 1.803 | 0.077 | 1.215 |
| Number of blades, $N_{\mathrm{b}}$ | **2** | 1.912 | – | – | – | – |
| | 3 | 1.879 | – | – | – | – |
| | 4 | 1.949 | – | – | – | – |
| Tip Mach number, $M_{\mathrm{tip}}$ | **0.233** | 1.912 | – | – | – | – |
| | 0.333 | 1.492 | – | – | – | – |
| | 0.433 | 1.343 | – | – | – | – |

### B1 Effect of rotor solidity

The effect of solidity was examined by varying the blade chord distribution of each of the three baseline rotors by ±10 %, while retaining the rotor radius, blade number, and other geometric parameters. This produces a corresponding ±10 % variation in rotor solidity, $\sigma$. For each case, the operating condition was adjusted to maintain DL = 100 N m$^{-2}$, i.e. the rotational speed was adjusted for the two UAV-scale rotors, whereas the collective pitch was trimmed for the HSR. Furthermore, the sectional lift coefficient was corrected for compressibility using the Prandtl–Glauert transformation (Glauert, 1928),

$$C_{\mathrm{l,\,compressible}} = \frac{C_{\mathrm{l,\,incompressible}}}{\sqrt{1-M^2}}, \tag{B2}$$

where $M$ is the local Mach number. While this correction is applied to the sectional lift coefficient; the underlying FVM formulation remains potential-flow-based and does not resolve viscous effects. Figure B1 compares the normalised, time-averaged induced velocity profiles for the three baseline rotors and their respective solidity variations. In the region upstream of the rotor disk, the profiles show the same ordering with solidity:

$$\left(\frac{V_{\mathrm{ind}}}{V_{\mathrm{tip}}}\right)_{+10\,\%\sigma} > \left(\frac{V_{\mathrm{ind}}}{V_{\mathrm{tip}}}\right)_{\mathrm{baseline}\,\sigma} > \left(\frac{V_{\mathrm{ind}}}{V_{\mathrm{tip}}}\right)_{-10\,\%\sigma}. \tag{B3}$$

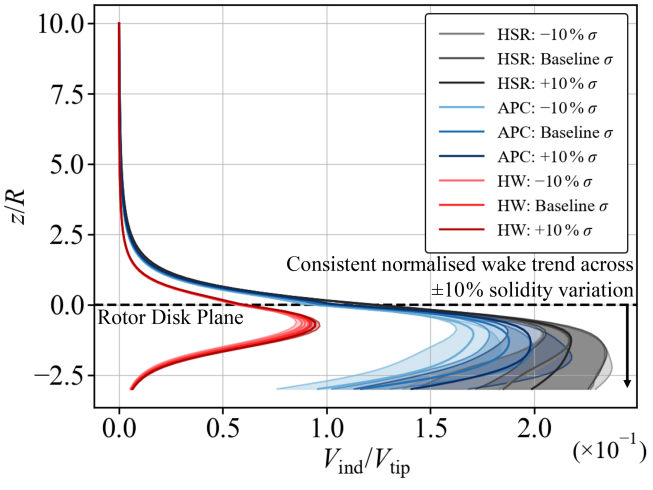


**Figure B1.** Time-averaged induced velocity normalised by rotor-tip speed, $V_{\mathrm{ind}}/V_{\mathrm{tip}}$, along the rotational axis of the rotor, $z/R$. Shown are the Harrington single-rotor (HSR), APC 12 × 6E propeller, and Hobbywing 2480 (HW) propeller in hover at DL = 100 N m$^{-2}$. For each rotor, the blade chord distribution is varied by ±10 %, with the operating condition adjusted to maintain the prescribed disk loading.

Although changing solidity alters the magnitude of the normalised induced velocity downstream of the rotors, the overall axial trends remain broadly comparable within each rotor configuration. The corresponding potential aerodynamic quiet-zone threshold locations are near similar across the cases on the rotor upstream, as shown in Table B1. Thus, the profiles indicate a degree of similarity at equal DL, while also indicating the existence of minor variations in the resulting threshold locations.

### B2 Effects of blade number and tip Mach number

The influence of blade number was investigated using the HSR by varying the baseline blade count from $N_{\mathrm{b}} = 2$ to $N_{\mathrm{b}} = 3$ and $N_{\mathrm{b}} = 4$. The original chord distributions and rotational speed were retained, and collective pitch was adjusted to maintain DL = 100 N m$^{-2}$. Figure B2a shows that the normalised induced velocity profiles remain broadly comparable across the three blade counts, revealing a similar effect that the modification to rotor solidity had on the induced velocity profiles – in principle, change in blade number effectively modifies the rotor solidity. The corresponding minimum axial locations for the potential aerodynamic quiet-zone threshold are also relatively close, although small differences remain (Table B1). This suggests that, for the blade-number range considered, the overall upstream velocity profile is less sensitive to blade count.

The effect of the rotor tip Mach number was examined separately for the HSR while the rotor geometry parameters were retained at the baseline values. Figure B2b shows the induced velocity trends at the rotational axis of the rotor for three different tip Mach numbers: starting from the baseline value $M_{\mathrm{tip}} = 0.233$, two cases were considered at $M_{\mathrm{tip}} = 0.333$ and $M_{\mathrm{tip}} = 0.433$. The operating condition was adjusted using collective pitch to maintain the prescribed disk loading. The compressibility correction (Eq. B2) was also included in the sectional lift calculation. As shown in Fig. B2, the normalised induced velocity profiles remain broadly comparable upstream of the rotor, while exhibiting a significant departure from the solidity effects in the minimum axial location associated with the $V_{\mathrm{ind}}/V_{\mathrm{tip}} = 0.01$ threshold. This $(z/R)_{\mathrm{min}}$ reduces from 1.912 at the baseline tip Mach number to 1.492 and 1.343 for the higher Mach numbers, respectively (see Table B1). The HSR is a full-scale rotor that operates at a fixed angular velocity, where the thrust condition is typically varied by adjusting the rotor collective pitch. Consequently, the operating tip Mach number remains constant, rendering this parameter sweep a purely numerical investigation rather than a study representative of physically viable full-scale rotor operations. Conversely, for UAV-scale variable RPM systems, variations to the angular speed do alter the tip Mach number. However, the typical range of operating conditions of these systems invariably produce Mach numbers within the same order of magnitude, and the result-

ing induced velocity solution exhibits only a weak sensitivity to these changes, especially in the upstream regions of the rotor where candidate sensor placement locations exist.

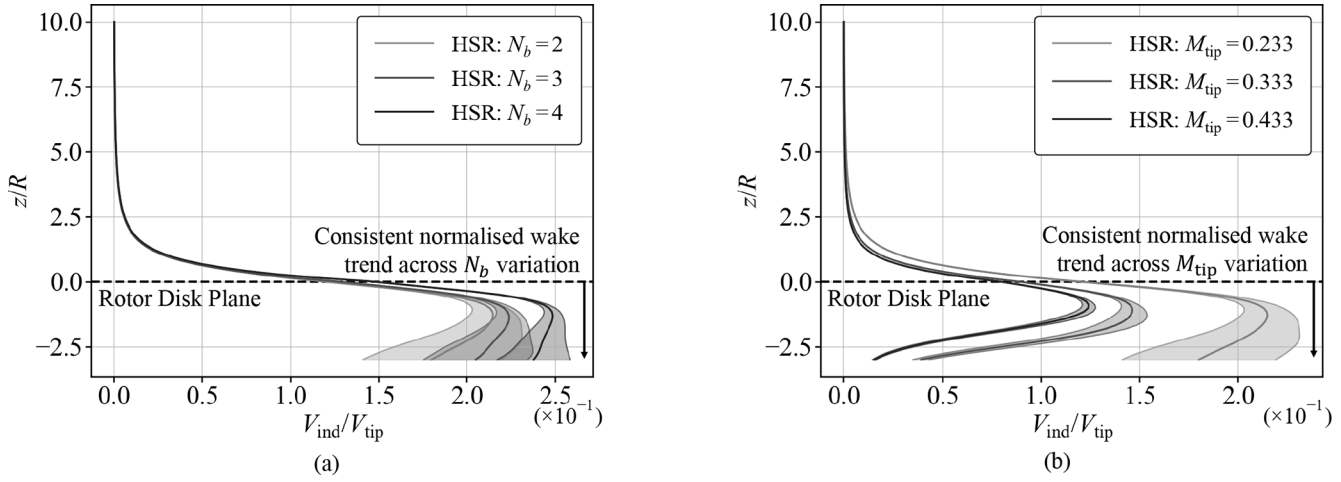


**Figure B2.** Comparison of time-averaged induced velocity normalised by rotor-tip speed ($V_{ind}/V_{tip}$) along the rotational axis of the rotor ($z/R$) for the HSR in hover at DL = 100 N m$^{-2}$, considering variations in **(a)** blade number ($N_b$) and **(b)** tip Mach number ($M_{tip}$).

Rooted in the momentum theory relation between the ideal hover induced velocity and $\sqrt{DL}$, alongside the weak sensitivity of the normalised induced velocity distribution to the rotor geometry and flow parameters, disk loading (DL) serves as a first-order accurate parameter for comparing rotor-induced flow across scales. The notable variations observed in the axial induced velocity profiles are confined to the rotor downstream, and do not influence the rotor upstream across different cases tested. This strengthens the use of DL as a simplified scaling parameter for investigating potential aerodynamic quiet-zones in different rotor systems for in situ meteorological measurements, without the necessity for exhaustive, case-specific aerodynamic testing.

## Appendix C: Validation of the in-house FVM model

The current FVM implementation was validated for steady and unsteady flow conditions by the authors Narayanan and Govindarajan (2024), and the key results are summarised here. Three different validation scenarios (aside from the one presented in the main document; see Fig. 9) were considered:

1. Power polar (thrust vs. power) prediction for the full-scale Harrington single and coaxial-rotors (Harrington, 1951) – steady flow
2. Rotor performance characteristics prediction (thrust and power as a function of angular speed) for the UAV-scale APC single-rotor (Brandt et al., 2015) – steady flow
3. Pitch rate study of the full-scale Carpenter–Fridovich single-rotor (Carpenter and Fridovich, 1953) – unsteady flow

### C1 Harrington experiments

The Harrington single and coaxial-rotor systems (Harrington, 1951) are 2-bladed, constant chord (0.46 m), untwisted, full-scale helicopter rotors; the rotor radius ($R = 3.81$ m), with an 18 %$R$ root cut-out length, and the blade sections are standard NACA 0012 airfoils. The vertical separation between the rotors of the coaxial configuration is 20 % $R$. The rotors from the original experiments were thickness-tapered along the span of the blade, while the current FVM implementation utilised a constant drag coefficient across the rotor, a strategy implemented in prior studies (Syal and Leishman, 2012). Figure C1a depicts the power polar for the Harrington single (blue) and coaxial-rotors (orange). Blade loading coefficient ($C_T/\sigma$) is chosen as the independent parameter in place of rotor thrust, to emphasise the lift loading on the blades. The solid lines correspond to the FVM results, and the circular markers represent the original experimental results (Harrington, 1951). The single-rotor was operated at 200 RPM (20.96 rad s$^{-1}$) and the coaxial-rotors were operated at 300 RPM (31.36 rad s$^{-1}$) across all the blade loading conditions, and the systems were trimmed to the target thrust, and zero in-plane moments by varying the rotor collectives. It can be observed that the FVM predictions agree well with the original experimental results, lending confidence in the developed FVM model; deviation in the results for lower thrust values could be attributed to the use of a constant drag coefficient in place of the tapered thickness rotor as in the original experiments.

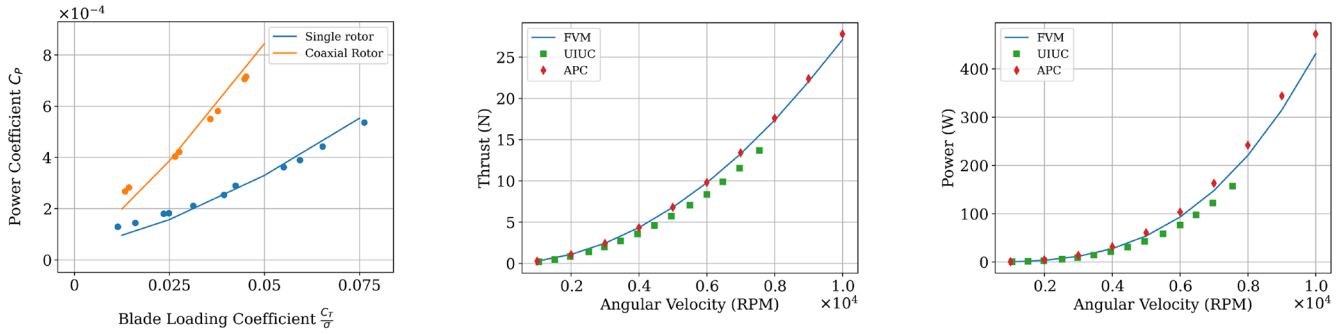


**Figure C1.** Validation of the developed FVM model for steady flow cases: **(a)** Harrington Polar Power; **(b)** APC, Thrust vs. RPM; **(c)** APC, Power vs. RPM.

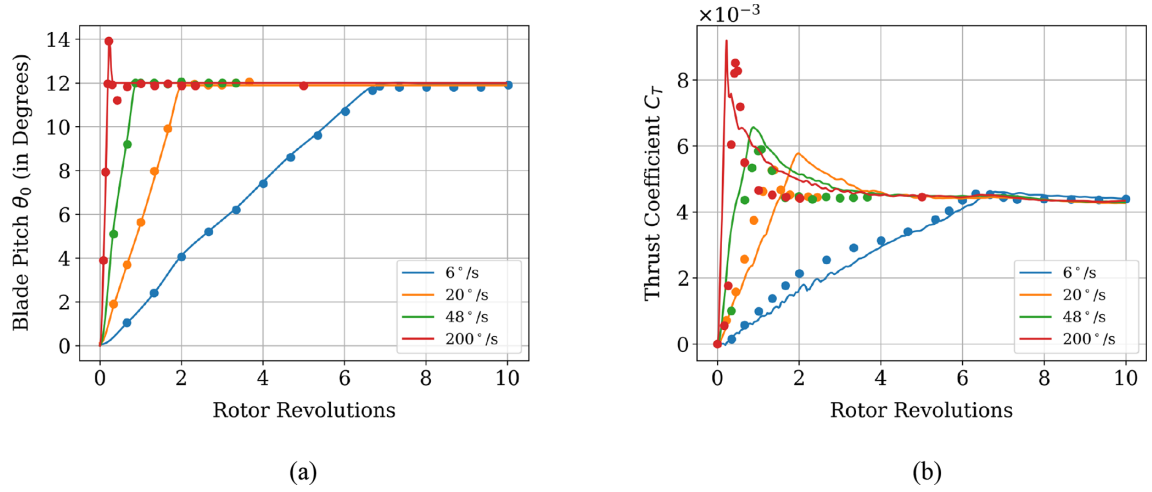


**Figure C2.** Validation of the developed FVM model for the unsteady flow case: **(a)** time history of rotor blade pitch; **(b)** time history of rotor thrust coefficient.

## C2 APC 12 × 6E single-rotor studies

The APC propeller is a UAV-scale 2-bladed rotor of radius ($R = 0.15$ m), with the root cut-out measuring 18.3 %$R$. The span-wise chord and twist distributions of the rotor are detailed in a previous work by the authors Narayanan and Govindarajan (2024). The thrust and power variations against rotor RPM were studied for the APC single-rotor, as shown in Fig. C1b and c, respectively. NACA 0012 airfoil with a modified zero-lift angle of attack ($\alpha = -2\,^\circ$) and drag coefficient ($C_d = 0.012$), was used as a surrogate to the actual airfoil sections used in the APC rotor. The fixed pitch APC rotor was treated as a rotor with a constant collective. It was observed that the FVM results were in good agreement with the UIUC and APC results (Brandt et al., 2015; APC Propellers, 2026) across all angular speeds (RPM), thereby validating the performance of the FVM model for steady problems for small-scale UAVs, in addition to the Harrington rotor problem.

## C3 Carpenter–Fridovich experiments

Carpenter–Fridovich experiments (Carpenter and Fridovich, 1953) were originally carried out to study the thrust response to rapidly pitching rotors. The rotor is a 2-bladed, untwisted, radius ($R = 5.79$ m), full-scale helicopter rotor, with a root cut-out of 20 %$R$, and constant chord of 0.25 m. To validate the FVM model for unsteady conditions, the pitch input from the original experiments was reproduced in the FVM model, for various pitch rates (6 to 200 $^\circ\,s^{-1}$) to increase the blade pitch from 0 to 12 °. The time history of the pitch rate input is shown in Fig. C2a. The highest pitch rate in Fig. C2a (200 $^\circ\,s^{-1}$, red) indicates an overshoot in pitch, which occurred due to the torsional response in the original experimental setup. The numerical formulation did not include the effects of structural dynamics, and therefore, the pitch input was mimicked as in the experiment. It can be inferred from the thrust response of the system (Fig. C2b) that the FVM model captures the variation in thrust coefficient reasonably

well in comparison to the original experiments, for all the pitch rates. For the highest pitch rate, the peak increase in the coefficient of thrust to nearly twice the steady state thrust value is also predicted well by the FVM model, adding to the reliability of the model in solving unsteady problems.

## Appendix D: Sensitivity of induced velocity predictions to numerical parameters in the FVM model

To assess the influence of the numerical settings such as discretisation and number of wake turns among others, on the induced velocity predicted by the FVM model, a sensitivity study was conducted on the APC $12 \times 6$E single-rotor by varying each parameter, one at a time, while retaining the remaining parameters at their baseline values. The analysis focuses on the region above the rotor plane, which is of primary interest for sensor placement and the induced velocity was evaluated along the axis of rotation of the rotor over the range $z/R = -3$ to 10.

Table D1 lists the parameter values considered in the study, with the baseline settings indicated in bold. In the current FVM implementation, the wake-age increment and vortex-segment length discretisation are held equal, i.e. $\Delta\psi = \Delta\zeta$. The time step for a given flight condition is also determined by the wake-age increment through $\Delta t = \Delta\psi/\Omega$, with the angular increment expressed in radians. Consequently, these discretisation settings are not varied independently.

**Table D1.** Values of the various numerical parameters examined in the sensitivity study of the APC single-rotor FVM simulations. Baseline settings are indicated in bold.

| Parameters | Values considered | | | |
|---|---|---|---|---|
| Wake turns, $N_{\text{turns}}$ | 4 | **6** | 8 | 10 |
| Wake-age increment, $\Delta\psi$ (°) | 2.5 | 5 | **10** | 15 |
| Core-radius-to-blade-chord ratio, $r_c / c$ | 0.005 | **0.010** | 0.015 | 0.020 |
| Number of vortex segments, $N_{\text{seg}}$ | 10 | 20 | 30 | **40** |
| Post-processing grid | $50 \times 50$ | **100 x 100** | | |

The baseline configuration comprised six retained wake turns, a wake discretisation increment of 10°, 40 vortex segments, a core-radius-to-blade-chord ratio of 0.01, and a $100 \times 100$ Cartesian post-processing grid. The sensitivity cases were evaluated for the APC $12 \times 6$E single-rotor in hover at a representative $\text{DL} = 200\,\text{N}\,\text{m}^{-2}$. For each case, the mean induced velocity and its associated $1\sigma$ variation were evaluated over 10 revolutions of the converged solution. Changes in the numerical settings resulted in disk-loading variations of no more than $\pm 10\,\%$, owing to changes in wake-induced effects that influence the local angle of attack and, consequently, the blade loading. The resulting induced velocity profiles are compared in Fig. D1.

1. Fig. D1a depicts the effect of changing the number of retained wake turns from four to ten, with six turns as the baseline, on the induced velocity profile. The predicted profiles are nearly coincident above the rotor plane. Increasing the number of retained turns beyond the baseline produces negligible change in this region, while differences are more apparent below the rotor plane, with the lowest value exhibiting significant decay closer to the rotor plane. However, these downstream trends evidently do not translate back to the upstream regions where possible sensor placement locations exist, and hence, Six wake turns are therefore considered for all simulations.

2. Fig. D1b shows the effect of the wake-age increment on the induced velocity characteristics. The profiles remain closely matched above the rotor plane for increments ranging from 2.5 to 15 °. While differences are noticeable below the rotor plane, the overall trends remain similar, largely within the $1\sigma$ fluctuations across the cases. The 10 ° baseline therefore provides consistent induced velocity predictions in the region of interest.

3. Fig. D1c compares the induced velocity profile obtained with core-radius-to-blade-chord ratios ranging from 0.005 to 0.020. The induced velocity profiles exhibit no significant variation above the rotor plane, with negligible differences below it, including a stable $1\sigma$ band. The predicted velocity in the upstream region is thus weakly sensitive to this parameter over the range considered, and the baseline value is retained for all simulations.

4. Fig. D1d shows the influence of the number of vortex segments on the induced velocity distribution. The variation in the rotor upstream is inconsequential, while differences are more apparent below the rotor plane when fewer segments are used. The 40-segment baseline gives consistent predictions without increasing the computational cost, and is hence utilised for all simulations.

5. Finally, Fig. D1e compares the induced velocity profile obtained using $50 \times 50$ and $100 \times 100$ Cartesian post-processing grids. The velocity profiles are almost identical over the region considered, particularly above the rotor plane, indicating that increasing the grid resolution from $50 \times 50$ to $100 \times 100$ has little influence on the predicted axial velocity trends. However, considering the different flight conditions, the more conservative $100 \times 100$ grid was employed for robustness.

Together, the five sensitivity studies illustrate that the mean induced velocity profiles above the rotor plane are weakly affected by the numerical parameter variations considered. Although differences are more noticeable below the rotor plane in certain parameter sweeps, the overall trends remain similar across the tested cases. The maximum excursion of the instantaneous induced velocity from its mean

value, evaluated over the ten converged rotor revolutions, was 6.237 %, across all cases. This excursion describes the temporal variation of the computed solution and is not, by itself, a measure of numerical discretisation uncertainty. Overall, the results support the use of the baseline settings for examining the general induced velocity trends in the regions relevant to sensor placement.

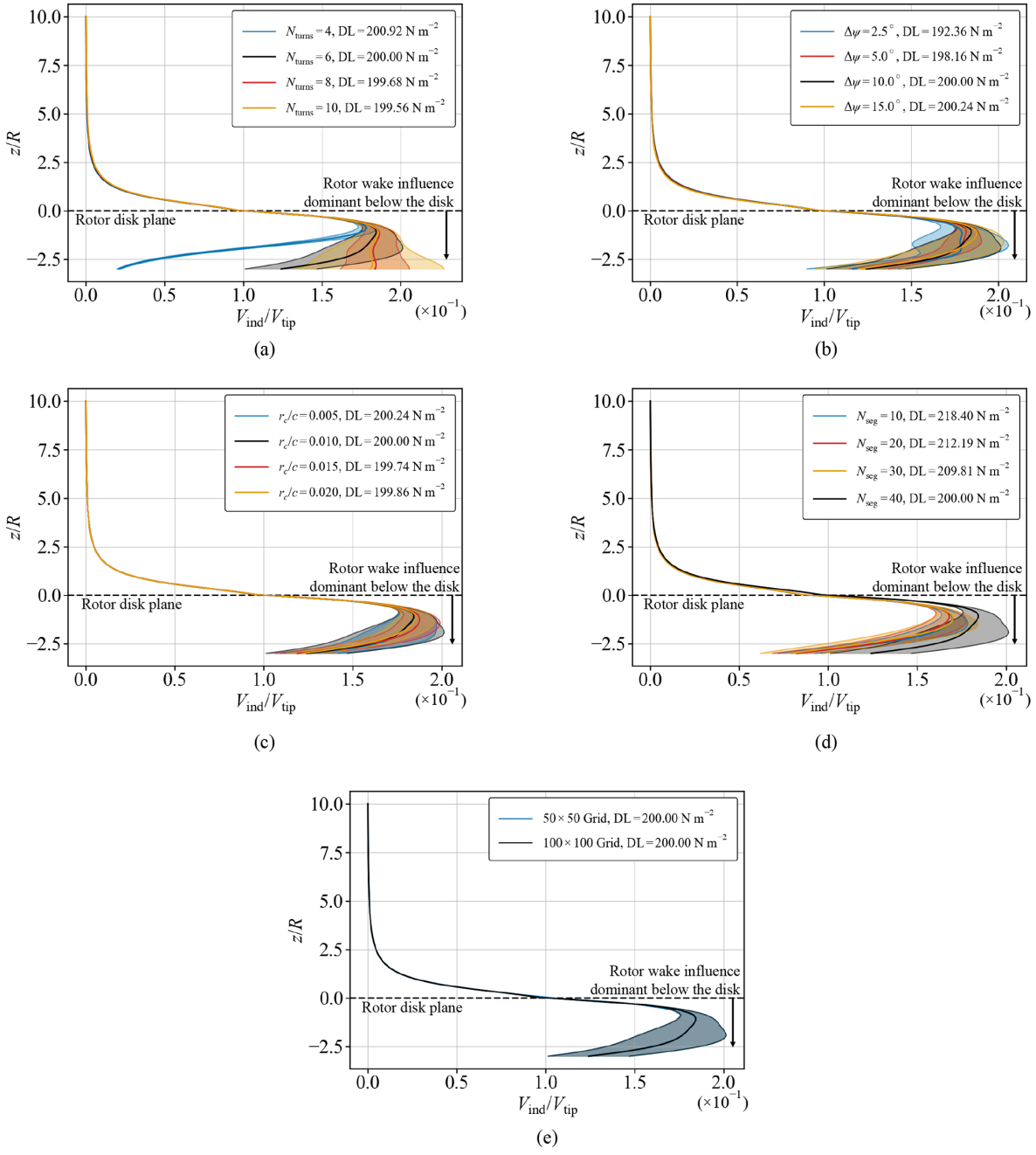


**Figure D1.** Sensitivity of numerical parameters to the induced-velocity field predictions for the APC single-rotor in hover, operating at a disk loading of 200 N m$^{-2}$: **(a)** number of wake turns ($N_{turns}$); **(b)** wake discretisation ($\Delta\psi$); **(c)** initial vortex core radius-to-blade chord ratio ($r_c$ / $c$); **(d)** number of blade segments ($N_{seg}$); and **(e)** grid sensitivity. The coloured solid curves represent the mean induced-velocity profiles, and the corresponding shaded regions indicate the 1$\sigma$ variation.

*Data availability.* The experimental and simulation data supporting the findings of this study are available from the reader upon request. The authors welcome data sharing, and access will be provided based on the intended scope and context of use to ensure data integrity and prevent misinterpretation.

*Author contributions.* Ashish Pastay: Investigation; Software; Formal analysis; Visualization; Writing – original draft; Writing – review and editing. Shrivathsan Narayanan: Methodology; Investigation; Formal analysis; Writing – original draft; Writing – review and editing. Bharath Govindarajan: Conceptualization; Methodology; Supervision; Formal analysis; Writing – review and editing.

*Competing interests.* The contact author has declared that none of the authors has any competing interests.

*Disclaimer.* Publisher's note: Copernicus Publications remains neutral with regard to jurisdictional claims made in the text, published maps, institutional affiliations, or any other geographical representation in this paper. The authors bear the ultimate responsibility for providing appropriate place names. Views expressed in the text are those of the authors and do not necessarily reflect the views of the publisher.

*Acknowledgements.* The authors would like to thank Shivaani VS, Project Associate at the Geophysical Flows Lab, Indian Institute of Technology Madras, Chennai, India, for her assistance with the in-house validation experiments.

Figure 1 was enhanced using a generative artificial intelligence tool to improve visual clarity and presentation quality. The AI tool was used solely for graphical refinement and did not generate, modify, or influence any scientific content, data, interpretation, or conclusions presented in this study. All scientific content remains entirely the responsibility of the authors.

*Review statement.* This paper was edited by Jianhuai Ye and reviewed by Amit Tandon and one anonymous referee.

## References

Ananthan, S. and Leishman, J. G.: Role of filament strain in the free-vortex modeling of rotor wakes, J. Am. Helicopter Soc., 49, 176–191, https://doi.org/10.4050/JAHS.49.176, 2004.

APC Propellers: 12 × 6E Propeller, https://www.apcprop.com/product/12x6e/?v=c86ee0d9d7ed (last access: 18 February 2026), 2026.

Basawanal, A., Laliberte, J., Borshchova, I., and Traub, L.: Experimental study of an ultrasonic anemometer for drone-based measurements, Drone Syst. Appl., 1, 1–19, https://doi.org/10.1139/dsa-2024-0035, 2025.

Bauknecht, A., Merz, C. B., Raffel, M., Landolt, A., and Meier, A. H.: Blade-tip vortex detection in maneuvering flight using the background-oriented schlieren technique, J. Aircraft, 51, 2005–2014, https://doi.org/10.2514/1.C032672, 2014.

Bhagwat, M. J. and Leishman, J. G.: Stability analysis of helicopter rotor wakes in axial flight, J. Am. Helicopter Soc., 45, 165–178, https://doi.org/10.4050/JAHS.45.165, 2000.

Bhagwat, M. J. and Leishman, J. G.: Accuracy of straight-line segmentation applied to curvilinear vortex filaments, J. Am. Helicopter Soc., 46, 166–169, https://doi.org/10.4050/JAHS.46.166, 2001.

Brandt, J. B., Deters, R. W., Ananda, G. K., Dantsker, O. D., and Selig, M. S.: UIUC Propeller Database, Vols 1–4, University of Illinois at Urbana-Champaign, https://m-selig.ae.illinois.edu/props/propDB.html (last access: 18 February 2026), 2015.

Brenner, J.: Inflow analysis for multi-rotors and the impact on sensor placement, M.S. thesis, Oklahoma State University, Stillwater, OK, USA, 172 pp., https://search.proquest.com/openview/be242e3239b8e72cd8ef8713c60152d5/1?pq-origsite=gscholar&cbl=18750&diss=y (last access: 7 November 2026), 2021.

Carpenter, P. J. and Fridovich, B.: Effect of a rapid blade-pitch increase on the thrust and induced-velocity response of a full-scale helicopter rotor, NACA Tech. Note TN 3044, National Advisory Committee for Aeronautics, https://ntrs.nasa.gov/citations/19930083686 (last access: 18 February 2026), 1953.

Cho, A., Kim, J., Lee, S., and Kee, C.: Wind estimation and airspeed calibration using a UAV with a single-antenna GPS receiver and pitot tube, IEEE T. Aero. Elec. Sys., 47, 109–117, https://doi.org/10.1109/TAES.2011.5705663, 2011.

Datta, A., Nixon, M. W., and Chopra, I.: Review of rotor loads prediction with the emergence of rotorcraft CFD, J. Am. Helicopter Soc., 52, 287–317, https://doi.org/10.4050/JAHS.52.287, 2007.

Draganfly: Commander 3 XL, https://draganfly.com/commander-3-xl/ (last access: 14 September 2026), 2026a.

Draganfly: Heavy Lift, https://draganfly.com/products/heavy-lift/ (last access: 14 September 2026), 2026b.

Faber, J., Gerding, M., and Köpnick, T.: Acquiring high-resolution wind measurements by modifying radiosonde sounding procedures, Atmos. Meas. Tech., 16, 4183–4193, https://doi.org/10.5194/amt-16-4183-2023, 2023.

Fujiwara, M., Sun, B., Reale, A., Cimini, D., Larosa, S., Borg, L., von Rohden, C., Sommer, M., Dirksen, R., Maturilli, M., Vömel, H., Kivi, R., Ingleby, B., Kramer, R. J., Demoz, B., Madonna, F., Carminati, F., Lewis, O., Candy, B., Thomas, C., Edwards, D., Noersomadi, Shimizu, K., and Thorne, P.: Justification for high-ascent attainment for balloon radiosonde soundings at GRUAN and other sites, Atmos. Meas. Tech., 18, 2919–2955, https://doi.org/10.5194/amt-18-2919-2025, 2025.

Gasch, P., Kasic, J., Maas, O., and Wang, Z.: Advancing airborne Doppler lidar wind profiling in turbulent boundary layer flow – an LES-based optimization of traditional scanning-beam versus novel fixed-beam measurement systems, Atmos. Meas. Tech., 16, 5495–5523, https://doi.org/10.5194/amt-16-5495-2023, 2023.

Ghirardelli, M., Kral, S. T., Müller, N. C., Hann, R., Cheynet, E., and Reuder, J.: Flow structure around a multicopter drone: a computational fluid dynamics analysis for sensor placement considerations, Drones, 7, 467, https://doi.org/10.3390/drones7070467, 2023.

Ghirardelli, M., Kral, S. T., Cheynet, E., and Reuder, J.: SAMURAI-S: Sonic Anemometer on a MUlti-Rotor drone for Atmospheric turbulence Investigation in a Sling load configuration, Atmos. Meas. Tech., 18, 2103–2124, https://doi.org/10.5194/amt-18-2103-2025, 2025.

Glauert, H.: The effect of compressibility on the lift of an aerofoil, Proc. R. Soc. Lond. A, 118, 113–119, https://doi.org/10.1098/rspa.1928.0039, 1928.

Harrington, R. D.: Full-scale-tunnel investigation of the static-thrust performance of a coaxial helicopter rotor, NACA Tech. Note TN 2318, National Advisory Committee for Aeronautics, https://ntrs.nasa.gov/citations/19930083001 (last access: 18 February 2026), 1951.

HobbywingDirect: XRotor MFP 2480 Propeller, https://www.hobbywingdirect.com/products/xrotor-2480-propeller (last access: 18 February 2026), 2026.

Hollenbeck, D., Nunez, G., Christensen, L. E., and Chen, Y. Q.: Wind measurement and estimation with small unmanned aerial systems (sUAS) using on-board mini ultrasonic anemometers, in: Proceedings of the 2018 International Conference on Unmanned Aircraft Systems (ICUAS), Dallas, TX, USA, 12–15 June 2018, 285–292, https://doi.org/10.1109/ICUAS.2018.8453418, 2018.

Hongfei Aviation Technology Co., Ltd.: HZH JY30 Rescue Drone – Can Carry a Variety of Pods, https://www.hongfeidrone.com/reasonable-price-agriculture-drone-business-plan-hzh-jy30-rescue-drone-can-carry-a-variety-of-pods-hongfei-product/ (last access: 7 November 2026), 2026a.

Hongfei Aviation Technology Co., Ltd.: HZH Y150 Transport Drone – 150KG Payload, https://www.hongfeidrone.com/hzh-y150-transport-drone-150kg-payload-product/ (last access: 14 September 2026), 2026b.

Inoue, J. and Sato, K.: Wind speed measurement by an inexpensive and lightweight thermal anemometer on a small UAV, Drones, 6, 289, https://doi.org/10.3390/drones6100289, 2022.

Jin, L., Ghirardelli, M., Mann, J., Sjöholm, M., Kral, S. T., and Reuder, J.: Rotary-wing drone-induced flow – comparison of simulations with lidar measurements, Atmos. Meas. Tech., 17, 2721–2737, https://doi.org/10.5194/amt-17-2721-2024, 2024.

JOUAV: CW-25E long endurance electric fixed-wing VTOL drone, https://web.archive.org/web/20260715075210/https://www.jouav.com/products/cw-25e.html (last access: 7 November 2026), 2026a.

JOUAV: CW-25H hydrogen-electric hybrid VTOL fixed-wing UAV, https://web.archive.org/web/20260518041604/https://www.jouav.com/products/cw-25h.html (last access: 7 November 2026), 2026b.

JOUAV: CW-30E hybrid gasoline & battery long flight time UAV, https://www.jouav.com/products/cw-30e.html (last access: 14 September 2026), 2026c.

JOUAV: CW-80E large commercial drone, https://www.jouav.com/products/cw-80e.html (last access: 14 September 2026), 2026d.

Lee, H., Sengupta, B., Araghizadeh, M. S., and Myong, R. S.: Review of vortex methods for rotor aerodynamics and wake dynamics, Adv. Aerodyn., 4, 20, https://doi.org/10.1186/s42774-022-00111-3, 2022.

Leishman, J. G.: Fundamentals of rotor aerodynamics, in: Principles of Helicopter Aerodynamics, 2nd edn., Cambridge University Press, Cambridge, UK, 55–114, ISBN 978-0-521-85860-1, https://www.cambridge.org/9780521858601 (last access: 7 November 2026), 2006a.

Leishman, J. G.: Unsteady airfoil behavior, in: Principles of Helicopter Aerodynamics, 2nd edn., Cambridge University Press, Cambridge, UK, 423–524, ISBN 978-0-521-85860-1, https://www.cambridge.org/9780521858601 (last access: 7 November 2026), 2006b.

Leishman, J. G.: Appendix A: Typical main rotor disk loadings and power loadings – Table A.1, in: Principles of Helicopter Aerodynamics, 2nd ed., Cambridge University Press, Cambridge, UK, 815, ISBN 978-0-521-85860-1, https://www.cambridge.org/9780521858601 (last access: 7 November 2026), 2006c.

Leishman, J. G., Bhagwat, M. J., and Bagai, A.: Free–vortex filament methods for the analysis of helicopter rotor wakes, J. Aircraft, 39, 759–775, https://doi.org/10.2514/2.3022, 2002.

LI-COR Environmental: LI-550 TriSonica Mini wind & weather sensor, https://www.licor.com/products/trisonica/LI-550-mini?category=Meteorology (last access: 7 November 2026), 2026.

Menapia Ltd.: MetSprite: UAV-based atmospheric measurement platform, Internet Archive Wayback Machine, https://web.archive.org/web/20260319142025/https://www.menapia.tech/metsprite-platform (last access: 7 November 2026), 2026.

Meteomatics: Meteodrones – Weather drones from Meteomatics, https://www.meteomatics.com/en/meteodrones-weather-drones/ (last access: 14 September 2026), 2026.

Modern Device: Wind Sensor Rev. P – Low Cost Anemometer, https://moderndevice.com/products/wind-sensor-rev-p (last access: 14 September 2026), 2026.

MotioNew: H100 Quadcopter, heavy payload drone, https://www.motionew.com/shop/multirotor-drone/h100-quadcopter-heavy-payload-drone/ (last access: 14 September 2026), 2026.

Narayanan, S. and Govindarajan, B.: Effects of gust on the aerodynamics of multi-rotors, Phys. Fluids, 36, 127169, https://doi.org/10.1063/5.0243421, 2024.

NW Blue: All Metal Pitot Tube for Airspeed Sensor (NWB-PIX057), https://nwblue.com/products/differential-pressure-pitot-tube (last access: 14 September 2026), 2026.

PCE Instruments: Windmessgerät PCE-FST-200-201, https://www.pce-instruments.com/deutsch/messtechnik/messgeraete-fuer-alle-parameter/windmessgeraet-windgeschwindigkeitsmesser-pce-instruments-windmessgeraet-pce-fst-200-201-det_5846441.htm (last access: 7 November 2026), 2026.

Pindado, S., Cubas, J., and Sorribes-Palmer, F.: The cup anemometer, a fundamental meteorological instrument for the wind energy industry, Sensors, 14, 21418–21452, https://doi.org/10.3390/s141121418, 2014.

Ritvanen, J., O'Connor, E., Moisseev, D., Lehtinen, R., Tyynelä, J., and Thobois, L.: Complementarity of wind measurements from co-located X-band weather radar and Doppler lidar, Atmos. Meas. Tech., 15, 6507–6519, https://doi.org/10.5194/amt-15-6507-2022, 2022.

Romani, G. and Casalino, D.: Rotorcraft blade-vortex interaction noise prediction using the Lattice–Boltzmann method, Aerosp. Sci. Technol., 88, 147–157, https://doi.org/10.1016/j.ast.2019.03.029, 2019.

Simon, N., Piqué, A., Snyder, D., Ikuma, K., Majumdar, A., and Hultmark, M.: Fast-response hot-wire flow sensors for wind and gust estimation on UAVs, Meas. Sci. Technol., 34, 025109, https://doi.org/10.1088/1361-6501/ac9f5c, 2022.

Stoffelen, A., Pailleux, J., Källén, E., Vaughan, J. M., Isaksen, L., Flamant, P., Wergen, W., and Andersson, E.: The atmospheric dynamics mission for global wind field measurement, B. Am. Meteorol. Soc., 86, 73–88, https://doi.org/10.1175/BAMS-86-1-73, 2005.

sUAS News: JOUAV CW-20, https://www.suasnews.com/2016/04/jouav-cw-20/ (last access: 14 September 2026), 2016.

Syal, M. and Leishman, J. G.: Aerodynamic optimization study of a coaxial rotor in hovering flight, J. Am. Helicopter Soc., 57, 1–15, https://doi.org/10.4050/JAHS.57.042003, 2012.

Thielicke, W., Hübert, W., Müller, U., Eggert, M., and Wilhelm, P.: Towards accurate and practical drone-based wind measurements with an ultrasonic anemometer, Atmos. Meas. Tech., 14, 1303–1318, https://doi.org/10.5194/amt-14-1303-2021, 2021.

T-Motor: AT2317 long shaft UAV motor for outdoor 3D trainer & glider, https://store.tmotor.com/product/at2317-long-shaft-fixed-wing-motor.html (last access: 14 September 2026), 2026.

UAVOS: UVH 170 – 4-stroke gasoline engine helicopter, https://web.archive.org/web/20261008174812/https://www.uavos.com/products/vtols/uav-helicopter-uvh-170/ (last access: 7 November 2026), 2026.

Wilson, T. C., Brenner, J., Morrison, Z., Jacob, J. D., and Elbing, B. R.: Wind speed statistics from a small UAS and its sensitivity to sensor location, Atmosphere, 13, 443, https://doi.org/10.3390/atmos13030443, 2022.

Witte, B. M., Singler, R. F., and Bailey, S. C. C.: Development of an unmanned aerial vehicle for the measurement of turbulence in the atmospheric boundary layer, Atmosphere, 8, 195, https://doi.org/10.3390/atmos8100195, 2017.

Zanotti, A., Savino, A., Palazzi, M., Tugnoli, M., and Muscarello, V.: Assessment of a mid-fidelity numerical approach for the investigation of tiltrotor aerodynamics, Appl. Sci., 11, 3385, https://doi.org/10.3390/app11083385, 2021.